Commun. Comput. Phys.
doi: 10.4208/cicp.OA-2020-0244

Vol. **x**, No. x, pp. 1-33
xxx 20xx

Numerical Approximations of Phase Field Models using a General Class of Linear Time-Integration Schemes

Lizhen Chen[1], Zengyan Zhang[2] and Jia Zhao[2,*]

[1] *Beijing Computational Science Research Center, Beijing, P.R. China.*
[2] *Department of Mathematics & Statistics, Utah State University, Logan, UT, USA.*

Received 3 December 2020; Accepted (in revised version) 2 June 2021

Abstract. In this paper, we develop a new class of linear time-integration schemes for phase-field models. The newly proposed schemes extend the recently developed energy quadratization technique by introducing extra free parameters to further stabilize the schemes and improve their accuracy. The freshly proposed schemes have several advantages. First of all, they are rather generic such that they apply to most existing phase-field models in the literature. The resulted schemes are also linear in time, which means only a linear system needs to be solved during each time marching step. Thus, it significantly reduces the computational cost. Besides, they are unconditionally energy stable such that a larger time step size is practical. What is more, the solution existence and uniqueness in each time step are guaranteed without any dependence on the time step size. To demonstrate the generality of the proposed schemes, we apply them to several typical examples, including the widely-used molecular beam epitaxy (MBE) model, the Cahn-Hilliard equation, and the diblock copolymer model. Numerical tests reveal that the proposed schemes are accurate and efficient. This new family of linear and unconditionally energy stable schemes provides insights in developing numerical approximations for general phase field models.

AMS subject classifications: 65M06, 65M12, 65M70

Key words: Phase field, linear scheme, energy stable, Cahn-Hilliard, diblock copolymer, molecular beam epitaxy growth.

1 Introduction

As an approach to solve interfacial problems, the phase field model has witnessed its popularity in the past decade. It has been widely applied to various fields, including vesicle dynamics, crystal growth, microstructure evolution, brittle fracture, and many

*Corresponding author. *Email addresses:* lzchen@csrc.ac.cn (L. Chen), zengyan.zhang@usu.edu (Z. Zhang) jia.zhao@usu.edu (J. Zhao)

others in material science and engineering. In general, the phase field models are driven by dissipative mechanisms, where the free energy is decreasing in time for isothermal systems. When the temperature changes can't be ignored, entropy is usually considered instead. These could be better explained by embracing the generalized Onsager principle [37,38,53,59].

Generically, the dynamics of the phase field variable Φ, which may be a vector, takes the form of

$$\partial_t \Phi = -\mathcal{G}\frac{\delta E}{\delta \Phi}, \tag{1.1}$$

where E is the effective free energy in the system that could be a functional of the phase variable Φ and its high-order gradient terms. Here $\mathcal{G}$ is a semi positive-definite operator, known as the mobility operator. In other words, the triplet $(\Phi,\mathcal{G},E)$ uniquely determines a thermodynamically consistent phase field model. When there is no flux contribution from the boundary, the dynamics of the phase field model (1.1) satisfies the following energy dissipation law

$$\frac{dE}{dt} = \Big(\frac{\delta E}{\delta \Phi},\frac{\delta \Phi}{\delta t}\Big) = -\Big(\mathcal{G}\frac{\delta E}{\delta \Phi},\frac{\delta E}{\delta \Phi}\Big) \leq 0. \tag{1.2}$$

Here the inner product is defined by

$$(\mathbf{f},\mathbf{g}) = \sum_i \int_\Omega f_i g_i d\Omega.$$

In the literature, many existing thermodynamically consistent phase field models could be reformulated into the general form in (1.1), including the Allen-Cahn model, Cahn-Hilliard model, phase-field crystal model, molecular beam epitaxy growth model, surfactant model, diblock copolymer model, and many others [2,3,15,16,46].

Due to the extensive applications of phase field models in various fields, many novel approaches of developing numerical approximations for the phase field PDE models are introduced in the literature. However, most numerical schemes are tailed specifically for a particular model, making their applications restricted. Among the existing numerical schemes published in the literature, if the numerical algorithms preserving the energy dissipation property of (1.2) in the discrete or semi-discrete level, they are known as energy stable algorithms. Furthermore, if such energy-stable property does not depend on the choice of the time-step size, they are usually named unconditionally energy stable. Such unconditionally energy stable schemes are always desirable and sometimes mandatory for solving the phase field models numerically. The energy stability properties guarantee the numerical solution's stability in certain norms. Theoretically, the solution's existence and uniqueness can usually be derived based on the discrete energy dissipation law. Meanwhile, since the energy dissipation of (1.2) is an intrinsic physical property for phase field models, unconditionally energy stable schemes usually guarantee long time stability with large time marching steps, though we shall point out unconditionally energy stable schemes do not necessarily guarantee solution accuracy [50]. Thus high-order energy stable schemes are more desired than first-order ones.

Over the past few decades, many novel energy-stable schemes to solve the phase field models are proposed. At present, the commonly used methods include the convex splitting approach [12,17,18,27,47,48], stabilized implicit-explicit approach [6,36,44,49,52,56, 58,60], discrete gradient method, discrete energy variation approach, the invariant energy quadratization (IEQ) approach [54, 59], the scalar auxiliary variable (SAV) approach [42] and many others [4,8,13,24–26,31,34,35]. Next, we give a brief review. For details, please check the references cited and the references therein.

The convex splitting approach dates back to the seminal work by Eyre [18], where a generic unconditionally energy stable one-step scheme is developed for the phase field models. The Cahn-Hilliard equation is specifically used to illustrate the idea [18]. The convex splitting method's major novelty is splitting the nonlinear terms in the free energy into a summation of a convex and a concave part. Then the convex part is discretized implicitly, and the concave part is discretized explicitly. Thanks to convex functions' property, the resulted schemes could be shown to be unconditional energy stable and uniquely solvable without any dependence on the time step size. This idea has been widely applied to solve a great deal of phase field models, including the Cahn-Hilliard models, epitaxial growth model, and phase-field crystal models [12, 40, 47, 48]. Many improvements have been established ever since. In particular, convex splitting Runge-Kutta methods have been proposed to solve the phase-field models [45]. A predictor-corrector technique is utilized to improve the accuracy of the convex splitting method [19]. Moreover, the convex splitting idea has also been utilized to solve nonlocal models [23]. Meanwhile, by treating the convex term implicitly, it usually produces some nonlinear systems. This makes the calculation tricky, especially for long-time numerical simulation. For instance, iterative Newton's method has to be used for each time step. In addition, there is no systematical clue on how to split the free energies as a summation of a convex part and a concave part, making the applications of the convex splitting idea limited.

Meanwhile, a stabilization technique was introduced to solve phase field models, particularly the Allen-Cahn equation and Cahn-Hilliard equation [43]. The stabilized implicit-explicit technique is simple and easy to apply. Only the constant-coefficient equations need to be solved for each time step. However, in the stabilized implicit-explicit approach, the nonlinear function is treated full-explicitly. A stable term must be added to balance the influence of explicit terms in order to obtain the energy stability result, making this method conditionally energy stable. Besides, it needs a restriction on the explicit terms, i.e., the Hessian matrix of the explicit term should be bounded. Recently, Li, Qiao, and Tang [32, 33] constructed a new stabilization method to reduce or eliminate this assumption, but it is still conditionally stable.

In addition, there are several other widely used approaches for developing energy stable schemes for phase field models. One popular approach is the discrete gradient method, which has been widely utilized in solving Hamiltonian systems but also phase field models. Though the discrete gradient method preserves the energy dissipation for solving phase field models, the resulted numerical schemes are usually highly nonlinear. This makes the numerical algorithms computationally expensive to solve and adds a

substantial restriction on the time-step size for the solution's existence and uniqueness in each time step. The exponential time integrator (ETD) method is also exploited to solve phase field models effectively [14, 30]. Though the ETD schemes are efficient, a general theoretical framework is still lacking. Among many ETD schemes in literature for solving the phase field models, only several numerical schemes can be theoretically shown to be energy stable. When the nonlinear terms are polynomials, energy stable multistep schemes could be developed [11]. Unfortunately, the nonlinear terms in most of the phase field models are not polynomial, making the multistep strategy very limited. Note, besides preserving the energy dissipation property, the schemes are sometimes desired to preserve more features, such as the maximum principle of the solution and total mass conservation [7].

Recently, based on the Lagrange multiplier method [1, 24], Yang et al. [54, 55, 59] proposed the invariant energy quadratization (IEQ) method. By introducing auxiliary variables, the IEQ method transforms the original nonlinear potential function into a quadratic form of the new variables. Instead of solving the original PDE models, the IEQ method solves the equivalent PDE models in terms of the new variables. By doing so, the resulted numerical schemes are linear, unconditionally energy stable, and uniquely solvable for each time stepping without any dependence of the time step. This IEQ method has been widely applied to many phase field models. Notice it is necessary to assume that the quadratized nonlinear potential energy density, for instance, the double-well potential for the Cahn-Hilliard equation, is bounded from below. Besides, due to the special construction of quadratic functions, it involves solving complicated variable coefficient equations. Shen et al. [41] introduce a scalar auxiliary variable instead of a spatially-dependent variable. The proposed scalar auxiliary variable (SAV) approach is also linear and unconditionally energy stable. Besides, this method has the advantage that only the constant-coefficient equation needs to be solved. A regularization technique is introduced in [5] to further stabilize the IEQ schemes. Meanwhile, by combing the IEQ/SAV methods with the Runge-Kutta method and Gaussian collocation method, arbitrarily high-order unconditionally energy stable schemes for phase field models have been developed [20–22]. Recently, a relaxation technique is introduced to remedy the inconsistency issue of the modified energy and the original energy for the IEQ/SAV methods [28, 57].

In this paper, we improve the accuracy and stability of the IEQ method for solving the general phase field model (1.1) by proposing a new family of linear and unconditionally energy stable schemes that are partially inspired by the work [13,29,59]. The free parameters in the general scheme could be further tuned based on the specific phase field models to improve accuracy and stability. However, the optimal choice (dependence) of the free parameters on the particular free energies is still an open problem to be investigated. The proposed method opens a new approach to developing energy-stable schemes for phase field models. Besides, the proposed schemes have several other advantages. First of all, they are generic. It applies to most existing phase field models; the resulted schemes are linear in time. In each time marching step, only a linear system needs to be solved.

Also, the resulted schemes are unconditionally energy stable such that a larger time step size is practical to be used. Several examples are presented, including the widely-used molecular beam epitaxy (MBE) equation, the Cahn-Hilliard equation, and the diblock copolymer model. Numerical tests demonstrate that the proposed schemes are accurate and efficient. This new family of linear and unconditionally energy stable schemes provides insights into the numerical approximations for phase field models. This idea could also be applied to develop energy stable numerical schemes for thermodynamically consistent models that satisfy the second law of thermodynamics.

The rest of this paper is organized as follows. In Section 2, we reformulate the general phase field models into an equivalent form by introducing auxiliary variables. Then in Section 3, we introduce the time discretization technique to obtain the linear semi-discrete schemes; Afterward, we present its applications in several examples, including the MBE model, the Cahn-Hilliard model, and the diblock copolymer model to demonstrate the effectiveness of the newly proposed scheme. The numerical results are shown in Section 4. In the end, a brief conclusion is presented.

2 General phase field models and their energy dissipation structures

2.1 The general phase field model

First of all, we briefly recall the general formulation for phase field models that is based on the generalized Onsager principle [37, 38, 53, 59]. We use $\Phi=(\phi_1,\cdots,\phi_d)^T$ to denote the thermodynamic variables, with d the dimension. The kinetic equation in domain Ω, stemming from the Onsager linear response theory, is given by

$$\partial_t\Phi(\mathbf{x},t)=-\mathcal{G}\frac{\delta E}{\delta\Phi},\quad \text{in } \Omega, \tag{2.1a}$$

$$\mathcal{C}(\Phi(\mathbf{x},t))=0,\quad \text{on } \partial\Omega, \tag{2.1b}$$

where $\mathcal{C}$ is a trace operator, $\mathcal{G}$ is the mobility operator and $\frac{\delta E}{\delta\Phi}$ is the variational derivative of E, known as the chemical potential. In general, we can split the mobility operators into two parts: $\mathcal{G}=\mathcal{G}_a+\mathcal{G}_s$. Here $\mathcal{G}_s$ is a semi positive-definite operator that controls the irreversible dynamics and $\mathcal{G}_a$ is skew-symmetric operator that controls the reversible dynamics. The triplet $(\Phi,\mathcal{G},E)$ uniquely defines a thermodynamically consistent model. One intrinsic property of (2.1) owing to the thermodynamical consistency is the energy dissipation law

$$\begin{aligned}\frac{dE}{dt}&=\Big(\frac{\delta E}{\delta\Phi},\frac{\partial\Phi}{\partial t}\Big)+\dot{E}_{surf}\\&=-\Big(\frac{\delta E}{\delta\Phi},\mathcal{G}_s\frac{\delta E}{\delta\Phi}\Big)+\dot{E}_{surf},\end{aligned}$$

where $\dot{E}_{surf}$ is due to the boundary contribution. The bulk contribution with the dissipation property is given as

$$\dot{E}_{bulk} = -\Big(\frac{\delta E}{\delta \Phi}, \mathcal{G}_s \frac{\delta E}{\delta \Phi}\Big) \leq 0. \tag{2.2}$$

Several remarks follow as below.

Remark 2.1. When $\mathcal{G}_a = 0$, (2.1) is a purely dissipative system; while $\mathcal{G}_s = 0$, it is a purely dispersive system. $\dot{E}_{surf}$ vanishes only for suitable boundary conditions, which include periodic and certain physical boundary conditions.

Remark 2.2. When the mass, momentum, and total energy conservation are present in hydrodynamic models, these conservation laws are viewed as constraints imposed on the hydrodynamic variables. Then, the energy dissipation rate will have to be calculated subject to the constraints.

For simplicity of notation, we only focus on periodic boundary conditions in the rest of this paper. However, we emphasize that all of the results work for physical boundary conditions that result in $\dot{E}_{surf} = 0$. We call (2.1) the generalized Onsager form. Many phase-field models can be cast into the generalized Onsager form.

2.2 Model reformulation using the energy quadratization method

We next introduce a paradigm to derive energy-stable numerical approximations for models in generalized Onsager form (2.1). We illustrate the idea using the energy density e, i.e.,

$$E = \int_\Omega e(\phi, \nabla \phi) d\Omega, \tag{2.3}$$

where e contains a quadratic gradient term $\frac{1}{2}|\mathcal{L}^{\frac{1}{2}}\Phi|^2$ with $\mathcal{L}$ a self-adjoint linear differential operator. More general cases can be handled analogously. We transform the free energy density into a quadratic one by introducing an auxiliary variable

$$q = \sqrt{2\Big(e - \frac{1}{2}|\mathcal{L}^{\frac{1}{2}}\Phi|^2 + \frac{A_0}{|\Omega|}\Big)}, \tag{2.4}$$

where $A_0 > 0$ is constant such that q is a well defined real variable. Here we have assumed that $e - \frac{1}{2}|\mathcal{L}^{\frac{1}{2}}\Phi|^2$ has a lower bound. The total energy is rewritten as

$$E(\Phi, q) = \Big(\frac{1}{2}\Phi, \mathcal{L}\Phi\Big) + \Big(\frac{1}{2}q, q\Big) - A_0. \tag{2.5}$$

Assuming $q = q(\Phi, \nabla\Phi)$ and denoting

$$g(\Phi) = \frac{\partial q}{\partial \Phi}, \quad \mathbf{h}(\nabla\Phi) = \frac{\partial q}{\partial \nabla \Phi},$$

we reformulate (2.1) into an equivalent form

$$\begin{cases} \partial_t \Phi = -(\mathcal{G}_a + \mathcal{G}_s)\Big[\mathcal{L}\Phi + qg(\Phi) - \nabla\cdot(q\mathbf{h}(\Phi))\Big], \\ \partial_t q = g(\Phi):\partial_t\Phi + \mathbf{h}(\nabla\Phi):\nabla\partial_t\Phi, \end{cases} \tag{2.6}$$

along with the consistent initial condition

$$q|_{t=0} = \sqrt{2\Big(e - \frac{1}{2}|\mathcal{L}^{\frac{1}{2}}\Phi|^2 + \frac{A_0}{|\Omega|}\Big)}\Big|_{t=0}.$$

Now, instead of dealing with (2.1) directly, we develop energy-stable schemes for (2.6). The advantage of using model (2.6) over model (2.1) is that the energy density is transformed into a quadratic one as shown in (2.5).

2.3 Reformulated models in a compact form

Furthermore, we rewrite (2.6) into a compact form as

$$\partial_t \Psi = -\mathcal{N}(\Psi)\mathcal{B}\Psi, \quad \text{with} \quad \Psi = \begin{bmatrix} \Phi \\ q \end{bmatrix}, \quad \mathcal{B} = \begin{bmatrix} \mathcal{L} & 0 \\ 0 & 1 \end{bmatrix}, \tag{2.7a}$$

$$\mathcal{N}(\Psi) = \mathcal{A}^*(\mathcal{G}_a + \mathcal{G}_s)\mathcal{A}, \quad \mathcal{A} = (\mathbf{I}_d,\, g(\Phi) + \mathbf{h}(\Phi):\,\nabla)_{d,d+1}, \tag{2.7b}$$

where $\mathcal{A}^*$ is the adjoint operator of $\mathcal{A}$ and $\mathcal{B}$ is a self-adjoint operator. We name the compact form in (2.7) the Onsager-Q model. When $\dot{E}_{surf} = 0$, the energy dissipation law can be calculated as

$$\frac{dE(\Psi)}{dt} = \Big(\frac{\delta E}{\delta \Psi}, \frac{\partial \Psi}{\partial t}\Big) = -\Big(\mathcal{B}\Psi, \mathcal{N}(\Psi)\mathcal{B}\Psi\Big) = -\Big(\mathcal{A}\mathcal{B}\Psi, \mathcal{G}_s\mathcal{A}\mathcal{B}\Psi\Big) \le 0. \tag{2.8}$$

Remark 2.3. Reformulating (2.1) into (2.6) or (2.7) is called the energy quadratization (EQ) reformulation or method. It could be observed that (2.1) is equivalent to (2.6) and (2.7). Thus solving (2.6) or (2.7) will in turn solve (2.1). Note that the energy in the Onsager-Q model is quadratized so that we can develop a paradigm to derive linear, energy stable numerical schemes for the model.

2.4 Model reformulation for specific phase field models

To illustrate the generality of the energy quadratization method explained in the previous sub-section, we provide several specific examples of widely-used phase field models.

2.4.1 Cahn-Hilliard equation

First of all, we consider the widely used Cahn-Hilliard equation as an example that reads as

$$\phi_t = M\Delta\Big(-\varepsilon^2\Delta\phi+(\phi^2-1)\phi\Big). \tag{2.9}$$

Here ϕ represents the local volume difference between two phases, ε is a model parameter to control the interface width, and M is the mobility coefficient. The Cahn-Hilliard equation in (2.9) is a special case of the general phase field model in (2.1) with the triplet $(\phi,\mathcal{G},E)$ given as

$$\phi, \quad \mathcal{G}=-M\Delta, \quad E(\phi)=\int_\Omega\Big(\frac{\varepsilon^2}{2}|\nabla\phi|^2+\frac{1}{4}(\phi^2-1)^2\Big)d\Omega. \tag{2.10}$$

With the periodic boundary condition or any other proper boundary condition that can satisfy the flux free condition at the boundary, such as $\partial_{\mathbf{n}}\phi|_{\partial\Omega}=0$ and $\partial_{\mathbf{n}}\Delta\phi|_{\partial\Omega}=0$ (where $\mathbf{n}$ is the unit outward normal on the boundary), we have the mass conservation property

$$\frac{d}{dt}\int_\Omega\phi(\mathbf{x},t)d\Omega=0. \tag{2.11}$$

And the model is thermodynamically consistent, in the sense that its free energy is dissipative in time. As a matter of fact, we can calculate the free energy dissipation rate

$$\frac{dE}{dt}=\int_\Omega\frac{\delta E}{\delta\phi}\frac{\delta\phi}{\delta t}d\Omega=-\int_\Omega M\Big|\nabla\Big(-\varepsilon^2\Delta\phi+(\phi^2-1)\phi\Big)\Big|^2d\Omega. \tag{2.12}$$

After introducing the auxiliary variable and notations

$$q(\mathbf{x},t):=\frac{\sqrt{2}}{2}\Big(\phi^2-(1+\gamma)\Big), \quad g(\phi):=\frac{\partial q}{\partial\phi}=\sqrt{2}\phi,$$

with $\gamma>0$ a regularization parameter [5], the original Cahn-Hilliard equation (2.9) is transformed into

$$\begin{cases}\phi_t=M\Delta\Big[-\varepsilon^2\Delta\phi+\gamma\phi+qg(\phi)\Big],\\ q_t=g(\phi)\phi_t,\end{cases} \tag{2.13}$$

with consistent initial conditions

$$\begin{cases}\phi|_{t=0}=\phi_0,\\ q|_{t=0}=\dfrac{\sqrt{2}}{2}\Big(\phi_0^2-(1+\gamma)\Big).\end{cases} \tag{2.14}$$

The reformulated Cahn-Hilliard equation in (2.13) can be easily reformulated in the compact form of (2.7) as

$$\Psi_t=-\mathcal{N}(\Psi)\mathcal{B}\Psi, \quad \Psi=\begin{bmatrix}\phi\\ q\end{bmatrix}, \quad \mathcal{B}=\begin{bmatrix}-\varepsilon^2\Delta+\gamma & 0\\ 0 & 1\end{bmatrix}, \tag{2.15a}$$

$$\mathcal{N}(\Psi)=\mathcal{A}^*\mathcal{G}\mathcal{A}, \quad \mathcal{A}=(1,g(\phi)), \quad \mathcal{G}=-M\Delta. \tag{2.15b}$$

2.4.2 Phase field models for diblock copolymers

Next, we consider the phase field diblock copolymer model [9, 39]. With ϕ an order parameter representing the local concentration difference of the components, the diblock copolymer model reads as

$$\phi_t = M\Delta\Big(-\varepsilon^2\Delta\phi+(\phi^2-1)\phi\Big)-M\alpha(\phi-\bar{\phi}), \tag{2.16}$$

followed with the periodic boundary condition. Here $M>0$ is the mobility parameter, $\varepsilon>0$ and $\alpha>0$ are model parameters, and $\bar{\phi}$ is the volume-averaged value for ϕ, i.e. $\bar{\phi}=\frac{1}{|\Omega|}\int_\Omega \phi d\Omega$. It is easy to show that $\bar{\phi}$ is a constant, and the total mass for each component is conserved, i.e., $\frac{d}{dt}\int_\Omega \phi(\mathbf{x},t)d\Omega=0$.

One can easily show that the model (2.16) is a special case of the general phase field model in (2.1) with the triplet $(\phi,\mathcal{G},E)$ defined by

$$\phi,\quad \mathcal{G}=-M\Delta,\quad E(\phi)=\int_\Omega\Big(\frac{\varepsilon^2}{2}|\nabla\phi|^2+\frac{1}{4}(\phi^2-1)^2+\frac{\alpha}{2}|\nabla\psi|^2\Big)d\Omega, \tag{2.17}$$

where ψ is the solution for the problem $\Delta\psi=(\phi-\bar{\phi})$ with a periodic boundary condition. The energy dissipation rate can be calculated as

$$\frac{dE}{dt}=\int_\Omega\frac{\delta E}{\delta\phi}\frac{\delta\phi}{\delta t}d\Omega=-\int_\Omega M\Big|\nabla\Big(\varepsilon^2\Delta\phi-(\phi^2-1)\phi+\alpha\psi\Big)\Big|^2 d\Omega. \tag{2.18}$$

Similarly, we can reformulate the model (2.16) using the energy quadratization (EQ) method. We introduce the auxiliary variable $q=\frac{\sqrt{2}}{2}\big(\phi^2-(1+\gamma)\big)$ with $\gamma>0$ a regularization parameter [5], and the notation $g(\phi):=\frac{\partial q}{\partial\phi}=\sqrt{2}\phi$. The original phase field diblock copolymer model (2.16) is transformed into

$$\begin{cases}\phi_t = M\Big[\Delta\Big(-\varepsilon^2\Delta\phi+\gamma\phi+qg(\phi)\Big)-\alpha(\phi-\bar{\phi})\Big],\\ q_t = g(\phi)\phi_t,\end{cases} \tag{2.19}$$

with consistent initial conditions

$$\begin{cases}\phi|_{t=0}=\phi_0,\\ q|_{t=0}=\dfrac{\sqrt{2}}{2}\Big(\phi_0^2-(1+\gamma)\Big).\end{cases} \tag{2.20}$$

Also, one can easily rewrite the reformulated model in (2.19) into the compact form of (2.7) as

$$\Psi_t=-\mathcal{N}(\Psi)\mathcal{B}\Psi,\quad \Psi=\begin{bmatrix}\phi\\ q\end{bmatrix},\quad \mathcal{B}=\begin{bmatrix}-\varepsilon^2\Delta+\gamma-\alpha\Delta^{-1}(\bullet-\frac{1}{|\Omega|}\int_\Omega\bullet d\Omega) & 0\\ 0 & 1\end{bmatrix}, \tag{2.21a}$$

$$\mathcal{N}(\Psi)=\mathcal{A}^*\mathcal{G}\mathcal{A},\quad \mathcal{A}=(1,g(\phi)),\quad \mathcal{G}=-M\Delta. \tag{2.21b}$$

2.4.3 Phase field models for molecular beam epitaxy (MBE) growth

In the third example, we consider the MBE model with slope selection, given as

$$\phi_t = -M\Big(\varepsilon^2\Delta^2\phi - \nabla\cdot((|\nabla\phi|^2-1)\nabla\phi)\Big), \tag{2.22}$$

with periodic boundary condition. Here ϕ represents the epitaxy surface height, ε is a model parameter, and M is the mobility coefficient. We have the mass conservation property

$$\frac{d}{dt}\int_\Omega \phi(\mathbf{x},t)d\Omega = 0.$$

Similarly as previous examples, we can easily identify that the MBE model in (2.22) is a special case of the general phase field model in (2.1), with the triplet $(\phi,\mathcal{G},E)$ given by

$$\phi, \quad \mathcal{G}=M, \quad E(\phi)=\int_\Omega\Big(\frac{\varepsilon^2}{2}(\Delta\phi)^2+\frac{1}{4}(|\nabla\phi|^2-1)^2\Big)d\Omega. \tag{2.23}$$

The energy dissipation property is calculated as

$$\frac{dE}{dt}=\int_\Omega\frac{\delta E}{\delta\phi}\frac{\delta\phi}{\delta t}d\Omega=-\int_\Omega M\Big(\varepsilon^2\Delta^2\phi-\nabla\cdot((|\nabla\phi|^2-1)\nabla\phi)\Big)^2 d\Omega\le 0. \tag{2.24}$$

Therefore, one would like to propose discrete numerical schemes to preserve the properties: mass conservation and energy dissipation. By introducing the auxiliary variable $q=\frac{\sqrt{2}}{2}\big(|\nabla\phi|^2-(1+\gamma)\big)$ with $\gamma>0$ constant the regularization parameter [5], and the notation $\mathbf{G}(\nabla\phi):=\frac{\partial q}{\partial\nabla\phi}=\sqrt{2}\nabla\phi$, we can derive the equivalent form

$$\begin{cases}\phi_t=-M\Big[\varepsilon^2\Delta^2\phi-\gamma\Delta\phi-\nabla\cdot(q\mathbf{G}(\nabla\phi))\Big],\\ q_t=\mathbf{G}(\nabla\phi)\cdot\nabla\phi_t,\end{cases} \tag{2.25}$$

with consistent initial conditions

$$\begin{cases}\phi|_{t=0}=\phi_0,\\ q|_{t=0}=\dfrac{\sqrt{2}}{2}\Big(|\nabla\phi_0|^2-(1+\gamma)\Big).\end{cases} \tag{2.26}$$

In a similar manner, the compact form for the reformulated system in (2.25) is written as

$$\Psi_t=-\mathcal{N}(\Psi)\mathcal{B}\Psi, \quad \Psi=\begin{bmatrix}\phi\\ q\end{bmatrix}, \quad \mathcal{B}=\begin{bmatrix}\varepsilon^2\Delta^2-\gamma\Delta & 0\\ 0 & 1\end{bmatrix}, \tag{2.27a}$$

$$\mathcal{N}(\Psi)=\mathcal{A}^*\mathcal{G}\mathcal{A}, \quad \mathcal{A}=\Big(1,-\nabla\cdot(\bullet\mathbf{G}(\nabla\phi))\Big), \quad \mathcal{G}=M. \tag{2.27b}$$

3 Linear time-integration schemes for phase field models

In this section, we introduce a new family of second-order numerical schemes to solve the general model (2.7), which in turn solves the general gradient model. Then we apply it on several specific phase field models.

Consider the time domain $(0,T]$, and we discretize it into equally distanced intervals $0=t_0<t_1<\cdots<t_N=T$ with $t_i=i\frac{T}{N}$ and N a positive integer. Hence $t_i=i\Delta t$, $\Delta t=\frac{T}{N}$ the time-step size. Then we denote Ψ^{n+1} as the numerical solution/approximation for $\Psi(t_{n+1})$.

3.1 A new family of linear time-integration schemes

Now we are ready to introduce the main numerical scheme of this paper to solve the reformulated model (2.7) that is equivalent to the originally general phase field model (2.1).

Scheme 3.1 (A general second-order scheme)**.** *Suppose Ψ^{n-1} and Ψ^n are known, Ψ^{n+1} could be updated via the following scheme*

$$\frac{1}{\Delta t}\Big[(\theta+\frac{1}{2})\Psi^{n+1}-2\theta\Psi^n+(\theta-\frac{1}{2})\Psi^{n-1}\Big]=-\mathcal{N}(\overline{\Psi}^{n+\theta})\mathcal{B}\Psi^{n+\theta}, \tag{3.1}$$

where $\overline{\Psi}^{n+\theta}=(1+\theta)\Psi^n-\theta\Psi^{n-1}$ and the $\Psi^{n+\theta}$ can be approximated by one of the two cases.

- *Case 1: define $\Psi^{n+\theta}$ as*

$$\Psi^{n+\theta}=\theta\Psi^{n+1}+(1-\theta)\Psi^n+\beta\theta\Big[\Psi^{n+1}-2\Psi^n+\Psi^{n-1}\Big],\quad \theta\geq\frac{1}{2},\quad \beta\geq 0. \tag{3.2}$$

- *Case 2: define $\Psi^{n+\theta}$ as*

$$\Psi^{n+\theta}=\theta\Psi^{n+1}+(1-\theta)\Psi^n+(\theta-\frac{1}{2})(1-\theta)\Big[\Psi^{n+1}-2\Psi^n+\Psi^{n-1}\Big],\quad \frac{1}{2}\leq\theta\leq\frac{3}{2}. \tag{3.3}$$

Here the left side of (3.1) is a second-order approximation of $\partial_t\Psi$ at $t_{n+\theta}$, $\overline{\Psi}^{n+\theta}=(1+\theta)\Psi^n-\theta\Psi^{n-1}$ is a second-order extrapolation for Ψ at $t_{n+\theta}$, and $\Psi^{n+\theta}$ is a linear combination of Ψ^{n+1}, Ψ^n and Ψ^{n-1} as a second-order approximation for Ψ at $t_{n+\theta}$.

One immediately notice that both (3.2) and (3.3) are second-order approximation of Ψ at $t_{n+\theta}$. We note similar ideas have been used in [13,29]. Applying them to (3.1) would reduce to a semi-discrete scheme of second order in time for the reformulated model (2.7), which in turn solves the general phase field model (2.1).

Remark 3.1. For the Case 2 in (3.3), when $\theta=\frac{1}{2}$, scheme 3.1 reduces to a second-order scheme based on a semi-implicit Crank-Nicolson time discretization. In the meanwhile, when $\theta=1$,scheme 3.1 reduces to a second order semi-implicit BDF2 scheme. Also, if we choose $\beta=\frac{(\theta-\frac{1}{2})(1-\theta)}{\theta}$, Case 1 in (3.2) reduces to Case 2 in (3.3).

Consider the domain Ω. For any $\Psi_1,\Psi_2\in\left[L^2(\Omega)\right]^{d+1}$ with $d+1$ the dimension of Ψ's, and $A\in\mathbb{R}^{(d+1)\times(d+1)}$ positive definite, define the operator-induced norm of the vector function Ψ and inner products of the vector functions Ψ_1 and Ψ_2 as

$$\|\Psi\|_A^2=(\Psi,A\Psi),\quad \Big(\Psi_1,\Psi_2\Big)_A=\Big(\Psi_1,A\Psi_2\Big), \tag{3.4}$$

respectively, where $(\Psi_1,\Psi_2)=\int_\Omega\Psi_1\cdot\Psi_2 d\Omega$, $\forall\Psi_1,\Psi_2\in\left[L^2(\Omega)\right]^{d+1}$. With a little abuse of notations, we also utilize the notation above when A is semi positive definite, which will induce a semi-norm.

Then, we introduce the following two lemmas, which are essential to prove the energy stability of the proposed scheme in (3.1).

Lemma 3.1. *Given $\Psi^{n-1},\Psi^n,\Psi^{n+1}\in[L^2(\Omega)]^{d+1}$, and*

$$\Psi^{n+\theta}=\theta\Psi^{n+1}+(1-\theta)\Psi^n+\beta\theta\Big[\Psi^{n+1}-2\Psi^n+\Psi^{n-1}\Big],\quad \theta\geq\frac{1}{2},\quad \beta\geq 0, \tag{3.5}$$

and a semi positive definite operator $\mathcal{B}$, it holds that

$$\begin{aligned}&\Big(\mathcal{B}\Psi^{n+\theta},(\theta+\frac{1}{2})\Psi^{n+1}-2\theta\Psi^n+(\theta-\frac{1}{2})\Psi^{n-1}\Big)\\ =&\left\|\begin{bmatrix}\Psi^{n+1}\\ \Psi^n\end{bmatrix}\right\|_G^2-\left\|\begin{bmatrix}\Psi^n\\ \Psi^{n-1}\end{bmatrix}\right\|_G^2+\frac{1}{4}\left\|\Psi^{n+1}-2\Psi^n+\Psi^{n-1}\right\|_F^2,\end{aligned} \tag{3.6}$$

where the operators G and F are defined as

$$G=\Big(\frac{1}{4}\begin{bmatrix}\theta(2\theta+3) & -(\theta+1)(2\theta-1)\\ -(\theta+1)(2\theta-1) & \theta(2\theta-1)\end{bmatrix}+\frac{\theta\beta}{2}\begin{bmatrix}1 & -1\\ -1 & 1\end{bmatrix}\Big)\otimes\mathcal{B}, \tag{3.7a}$$

$$F=\Big(\theta(2\theta-1)+4\theta^2\beta\Big)\mathcal{B}, \tag{3.7b}$$

with $\otimes$ represents the Kronecker product.

Proof. It is easy to show that the matrix

$$\frac{1}{4}\begin{bmatrix}\theta(2\theta+3) & -(\theta+1)(2\theta-1)\\ -(\theta+1)(2\theta-1) & \theta(2\theta-1)\end{bmatrix}+\frac{\theta\beta}{2}\begin{bmatrix}1 & -1\\ -1 & 1\end{bmatrix} \tag{3.8}$$

is semi positive definite, given $\theta\geq\frac{1}{2}$ and $\beta\geq 0$. On the one hand, by calculating carefully, we can derive the left hand side of (3.6) as

$$\begin{aligned}&\Big(\mathcal{B}\Psi^{n+\theta},\Big(\theta+\frac{1}{2}\Big)\Psi^{n+1}-2\theta\Psi^n+\Big(\theta-\frac{1}{2}\Big)\Psi^{n-1}\Big)\\ =&\theta\Big(\theta+\frac{1}{2}\Big)(1+\beta)(\mathcal{B}\Psi^{n+1},\Psi^{n+1})-2\theta(1-\theta(1+2\beta))(\mathcal{B}\Psi^n,\Psi^n)\\ &+\theta\Big(\theta-\frac{1}{2}\Big)\beta(\mathcal{B}\Psi^{n-1},\Psi^{n-1})+\Big(-4\theta^2\beta-3\theta^2+\frac{\theta}{2}-\theta\beta+\frac{1}{2}\Big)(\mathcal{B}\Psi^{n+1},\Psi^n)\\ &+\theta\Big(2\theta\beta+\theta-\frac{1}{2}\Big)(\mathcal{B}\Psi^{n+1},\Psi^{n-1})+\Big(\frac{3}{2}\theta-\theta^2-\frac{1}{2}+\theta\beta-4\theta^2\beta\Big)(\mathcal{B}\Psi^n,\Psi^{n-1}).\end{aligned} \tag{3.9}$$

On the other hand, by plugging the expression of (3.7a) and (3.7b) into the right hand side of (3.6), we have

$$\begin{aligned}
&\frac{1}{4}\left\|\Psi^{n+1}-2\Psi^n+\Psi^{n-1}\right\|_F^2\\
=&\frac{\theta(2\theta-1)+4\theta^2\beta}{4}(\mathcal{B}\Psi^{n+1},\Psi^{n+1})+\big(\theta(2\theta-1)+4\theta^2\beta\big)(\mathcal{B}\Psi^n,\Psi^n)\\
&+\frac{\theta(2\theta-1)+4\theta^2\beta}{4}(\mathcal{B}\Psi^{n-1},\Psi^{n-1})-\big(\theta(2\theta-1)+4\theta^2\beta\big)(\mathcal{B}\Psi^{n+1},\Psi^n)\\
&+\frac{\theta(2\theta-1)+4\theta^2\beta}{2}(\mathcal{B}\Psi^{n+1},\Psi^{n-1})-\big(\theta(2\theta-1)+4\theta^2\beta\big)(\mathcal{B}\Psi^n,\Psi^{n-1}),
\end{aligned}\tag{3.10}$$

$$\begin{aligned}
&\left\|\begin{bmatrix}\Psi^{n+1}\\ \Psi^n\end{bmatrix}\right\|_G^2-\left\|\begin{bmatrix}\Psi^n\\ \Psi^{n-1}\end{bmatrix}\right\|_G^2\\
=&\frac{\theta(2\theta+3)+2\theta\beta}{4}(\mathcal{B}\Psi^{n+1},\Psi^{n+1})+\frac{\theta(2\theta-1)+2\theta\beta}{4}(\mathcal{B}\Psi^n,\Psi^n)\\
&-\frac{(\theta+1)(2\theta-1)+2\theta\beta}{2}(\mathcal{B}\Psi^{n+1},\Psi^n)-\frac{\theta(2\theta+3)+2\theta\beta}{4}(\mathcal{B}\Psi^n,\Psi^n)\\
&-\frac{\theta(2\theta-1)+2\theta\beta}{4}(\mathcal{B}\Psi^{n-1},\Psi^{n-1})+\frac{(\theta+1)(2\theta-1)+2\theta\beta}{2}(\mathcal{B}\Psi^n,\Psi^{n-1})\\
=&\frac{\theta(2\theta+3)+2\theta\beta}{4}(\mathcal{B}\Psi^{n+1},\Psi^{n+1})-\theta(\mathcal{B}\Psi^n,\Psi^n)-\frac{\theta(2\theta-1)+2\theta\beta}{4}(\mathcal{B}\Psi^{n-1},\Psi^{n-1})\\
&-\frac{(\theta+1)(2\theta-1)+2\theta\beta}{2}(\mathcal{B}\Psi^{n+1},\Psi^n)+\frac{(\theta+1)(2\theta-1)+2\theta\beta}{2}(\mathcal{B}\Psi^n,\Psi^{n-1}).
\end{aligned}\tag{3.11}$$

Therefore, we have

$$\begin{aligned}
&\left\|\begin{bmatrix}\Psi^{n+1}\\ \Psi^n\end{bmatrix}\right\|_G^2-\left\|\begin{bmatrix}\Psi^n\\ \Psi^{n-1}\end{bmatrix}\right\|_G^2+\frac{1}{4}\left\|\Psi^{n+1}-2\Psi^n+\Psi^{n-1}\right\|_F^2\\
=&\theta\Big(\theta+\frac{1}{2}\Big)(1+\beta)(\mathcal{B}\Psi^{n+1},\Psi^{n+1})-2\theta(1-\theta(1+2\beta))(\mathcal{B}\Psi^n,\Psi^n)\\
&+\theta\Big(\theta-\frac{1}{2}\Big)\beta(\mathcal{B}\Psi^{n-1},\Psi^{n-1})+\Big(-4\theta^2\beta-3\theta^2+\frac{\theta}{2}-\theta\beta+\frac{1}{2}\Big)(\mathcal{B}\Psi^{n+1},\Psi^n)\\
&+\theta\Big(2\theta\beta+\theta-\frac{1}{2}\Big)(\mathcal{B}\Psi^{n+1},\Psi^{n-1})+\Big(\frac{3}{2}\theta-\theta^2-\frac{1}{2}+\theta\beta-4\theta^2\beta\Big)(\mathcal{B}\Psi^n,\Psi^{n-1}).
\end{aligned}\tag{3.12}$$

Thus, (3.6) holds. This completes this proof. □

Lemma 3.2. *Given* $\Psi^{n-1},\Psi^n,\Psi^{n+1}\in[L^2(\Omega)]^{d+1}$, *and*

$$\Psi^{n+\theta}=\theta\Psi^{n+1}+(1-\theta)\Psi^n+\Big(\theta-\frac{1}{2}\Big)(1-\theta)\Big[\Psi^{n+1}-2\Psi^n+\Psi^{n-1}\Big],\quad \frac{1}{2}\le\theta\le\frac{3}{2},\tag{3.13}$$

and $\mathcal{B}$ a semi positive definite operator, it holds that

$$\begin{aligned}&\left(\mathcal{B}\Psi^{n+\theta},\left(\theta+\frac{1}{2}\right)\Psi^{n+1}-2\theta\Psi^{n}+\left(\theta-\frac{1}{2}\right)\Psi^{n-1}\right)\\&=\left\|\begin{bmatrix}\Psi^{n+1}\\ \Psi^{n}\end{bmatrix}\right\|_G^2-\left\|\begin{bmatrix}\Psi^{n}\\ \Psi^{n-1}\end{bmatrix}\right\|_G^2+\frac{1}{4}\left\|\Psi^{n+1}-2\Psi^{n}+\Psi^{n-1}\right\|_F^2,\end{aligned}$$

where the operators G and F are defined by

$$G=\left(\frac{1}{2}\left(\frac{3}{2}-\theta\right)\begin{bmatrix}1&0\\0&0\end{bmatrix}+\frac{1}{2}\left(\theta-\frac{1}{2}\right)\begin{bmatrix}4&-2\\-2&1\end{bmatrix}\right)\otimes\mathcal{B}, \tag{3.14a}$$

$$F=4\theta\left(\theta-\frac{1}{2}\right)\left(\frac{3}{2}-\theta\right)\mathcal{B}, \tag{3.14b}$$

with $\otimes$ represents the Kronecker product.

The proof of this lemma is very similar to the proof of the previous one. As a matter of fact, we can verify this lemma by replacing β in the previous proof with $\frac{(\theta-\frac{1}{2})(1-\theta)}{\theta}$.

Next, we are ready to present the major theorem of this paper.

Theorem 3.1. *The proposed scheme* 3.1 *with $\Psi^{n+\theta}$ defined either in* (3.2) *or* (3.3) *is unconditionally energy stable. In particular, they satisfy the energy dissipation law as*

$$\begin{aligned}&\left\|\begin{bmatrix}\Psi^{n+1}\\ \Psi^{n}\end{bmatrix}\right\|_G^2-\left\|\begin{bmatrix}\Psi^{n}\\ \Psi^{n-1}\end{bmatrix}\right\|_G^2+\frac{1}{4}\left\|\Psi^{n+1}-2\Psi^{n}+\Psi^{n-1}\right\|_F^2\\&\qquad+\Delta t\left(\mathcal{B}\Psi^{n+\theta},\mathcal{N}(\overline{\Psi}^{n+\theta})\mathcal{B}\Psi^{n+\theta}\right)=0,\end{aligned} \tag{3.15}$$

where, G and F are defined in (3.7a) *and* (3.7b) *for $\Psi^{n+\theta}$ in* (3.2)*, G and F are defined in* (3.14a) *and* (3.14b) *for $\Psi^{n+\theta}$ in* (3.3)*.*

Proof. The proof is straightforward. If we take inner product of Eq. (3.1) with $\mathcal{B}\Psi^{n+\theta}$ on both side, we will directly obtain (3.15), by taking advantages of (3.6), based on the choices of $\Psi^{n+\theta}$. In addition, the choices of G and F are based on the choices of $\Psi^{n+\theta}$. This completes the proof. □

Remark 3.2. Given $\mathcal{B}$ a positive definite operator, the proposed scheme 3.1 is uniquely solvable for any time step $\Delta t>0$ [59].

3.2 Linear time integration schemes for specific phase field models

We emphasize that the proposed scheme 3.1 is rather general so that it applies to various phase field models. In the rest of this section, we apply it to several specific cases to better explain its capability in developing energy stable schemes for phase field models.

In particular, we present three specific examples to illustrate the power of the proposed generic numerical technique, namely the Cahn-Hilliard equation, the diblock copolymer model, and the molecular beam epitaxy model that is one specific case of the Allen-Cahn type equations.

3.2.1 Numerical approximations for the Cahn-Hilliard equation

First of all, we focus on the Cahn-Hilliard equation given in (2.9). After energy quadratization, we have (2.13) with the consistent initial condition (2.14). Then, a new family of second-order schemes could be introduced by following the general strategy in scheme 3.1 as shown below.

Scheme 3.2. *Assuming that* (ϕ^n,q^n), *and* (ϕ^{n-1},q^{n-1}) *are already calculated with* $n\geq 1$, *we then compute* (ϕ^{n+1},q^{n+1}) *from the following temporal discrete system:*

$$\begin{aligned}&\frac{1}{\Delta t}\Big[\Big(\theta+\frac{1}{2}\Big)\phi^{n+1}-2\theta\phi^n+\Big(\theta-\frac{1}{2}\Big)\phi^{n-1}\Big]\\&=M\Delta\Big(-\varepsilon^2\Delta\phi^{n+\theta}+\gamma\phi^{n+\theta}+q^{n+\theta}g(\overline{\phi}^{n+\theta})\Big),\end{aligned}\tag{3.16a}$$

$$\begin{aligned}&\frac{1}{\Delta t}\Big[\Big(\theta+\frac{1}{2}\Big)q^{n+1}-2\theta q^n+\Big(\theta-\frac{1}{2}\Big)q^{n-1}\Big]\\&=g(\overline{\phi}^{n+\theta})\frac{1}{\Delta t}\Big[\Big(\theta+\frac{1}{2}\Big)\phi^{n+1}-2\theta\phi^n+\Big(\theta-\frac{1}{2}\Big)\phi^{n-1}\Big],\end{aligned}\tag{3.16b}$$

where $\overline{(\cdot)}^{n+\theta}=(1+\theta)(\cdot)^n-\theta(\cdot)^{n-1}$, $g(\phi)=\sqrt{2}\phi$, *and* $(\cdot)^{n+\theta}$ *is defined in either* (3.2) *or* (3.3).

Remark 3.3. In practice, we compute (ϕ^1,q^1) from the following first-order Euler scheme:

$$\frac{\phi^1-\phi^0}{\Delta t}=M\Delta\Big(-\varepsilon^2\Delta\phi^1+\gamma\phi^1+q^1g(\phi^0)\Big),\tag{3.17a}$$

$$\frac{q^1-q^0}{\Delta t}=g(\phi^0)\frac{\phi^1-\phi^0}{\Delta t}.\tag{3.17b}$$

Theorem 3.2. *The proposed scheme* 3.2 *is unconditionally energy stable, and it satisfies the following energy dissipation law*

$$E^{n+1}-E^n\leq-\Delta tM\int_\Omega\Big|\nabla\Big(\varepsilon^2\Delta\phi^{n+\theta}-\gamma\phi^{n+\theta}-(q^{n+\theta}\overline{\phi}^{n+\theta})\Big)\Big|^2d\Omega,\quad n\geq 1.\tag{3.18}$$

Here E^{n+1}, E^n *and* $\mathcal{B}$ *are defined as*

$$E^{n+1}=\Big\|\begin{bmatrix}\Psi^{n+1}\\ \Psi^n\end{bmatrix}\Big\|_G^2,\quad E^n=\Big\|\begin{bmatrix}\Psi^{n}\\ \Psi^{n-1}\end{bmatrix}\Big\|_G^2,\quad \mathcal{B}=\begin{bmatrix}-\varepsilon^2\Delta+\gamma & 0\\ 0 & 1\end{bmatrix},\tag{3.19}$$

with G defined in (3.7a) *for the case of* (3.2), *and G defined in* (3.14a) *for the case of* (3.3).

As the proof is similar to the one in Theorem 3.1, we omit it for brevity.

3.2.2 Numerical approximations for the phase field diblock-copolymer model

Next, we utilize the numerical idea to approximation the phase field diblock copolymer model is given in (2.16). After equivalent transformation using the energy quadratization method, we obtain (2.19) along with the consistent initial condition (2.20). Thus the proposed numerical strategy in scheme 3.1 applies as well. Following the general numerical strategy, a new family of second-order schemes for the diblock copolymer model could be introduced as follows.

Scheme 3.3. *Assuming that* (ϕ^n,q^n)*, and* (ϕ^{n-1},q^{n-1}) *are already calculated with* $n\geq 1$*, we then compute* (ϕ^{n+1},q^{n+1}) *from the following temporal discrete system:*

$$\begin{aligned}&\frac{(\theta+\frac{1}{2})\phi^{n+1}-2\theta\phi^n+(\theta-\frac{1}{2})\phi^{n-1}}{\Delta t}\\&=M\Big(\Delta\Big[-\varepsilon^2\Delta\phi^{n+\theta}+\gamma\phi^{n+\theta}+q^{n+\theta}g(\overline{\phi}^{n+\theta})\Big]+\alpha(\phi^{n+\theta}-\bar{\phi})\Big),\end{aligned}\tag{3.20a}$$

$$\begin{aligned}&\frac{(\theta+\frac{1}{2})q^{n+1}-2\theta q^n+(\theta-\frac{1}{2})q^{n-1}}{\Delta t}\\&=g(\overline{\phi}^{n+\theta})\frac{(\theta+\frac{1}{2})\phi^{n+1}-2\theta\phi^n+(\theta-\frac{1}{2})\phi^{n-1}}{\Delta t},\end{aligned}\tag{3.20b}$$

where $\overline{(\cdot)}^{n+\theta}=(1+\theta)(\cdot)^n-\theta(\cdot)^{n-1}$*,* $g(\phi)=\sqrt{2}\phi$ *and* $(\cdot)^{n+\theta}$ *is defined in either* (3.2) *or* (3.3)*.*

Remark 3.4. Similarly as the previous scheme, We compute (ϕ^1,q^1) from the following first-order Euler scheme:

$$\frac{\phi^1-\phi^0}{\Delta t}=M\Big(-\varepsilon^2\Delta^2\phi^1+\gamma\Delta\phi^1+\Delta(q^1g(\phi^0))-\alpha(\phi^1-\bar{\phi})\Big),\tag{3.21a}$$

$$\frac{q^1-q^0}{\Delta t}=g(\phi^0)\frac{\phi^1-\phi^0}{\Delta t}.\tag{3.21b}$$

The unconditional energy stability of this scheme directly follows the results in previous sections.

Theorem 3.3. *The proposed scheme* 3.3 *is unconditionally energy stable, and it satisfies the following energy dissipation law*

$$E^{n+1}-E^n\leq-\Delta tM\int_\Omega\Big|\nabla\Big(\varepsilon^2\Delta\phi^{n+\theta}-\gamma\phi^{n+\theta}-q^{n+\theta}g(\overline{\phi}^{n+\theta})+\alpha\psi^{n+\theta}\Big)\Big|^2d\Omega,\quad n\geq1,\tag{3.22}$$

where $\psi^{n+1}:=(-\Delta)^{-1}(\phi^{n+1}-\overline{\phi})$*. Here* E^{n+1}*,* E^n *and* $\mathcal{B}$ *are defined as*

$$E^{n+1}=\left\|\begin{bmatrix}\Psi^{n+1}\\ \Psi^n\end{bmatrix}\right\|_G^2,\quad E^n=\left\|\begin{bmatrix}\Psi^n\\ \Psi^{n-1}\end{bmatrix}\right\|_G^2,\quad \mathcal{B}=\begin{bmatrix}-\varepsilon^2\Delta+\gamma & 0\\ 0 & 1\end{bmatrix},\tag{3.23}$$

with G defined in (3.7a) *for the case of* (3.2)*, and G defined in* (3.14a) *for the case of* (3.3)*.*

As the proof is similar to the one in Theorem 3.1, we thus omit the details. In addition, the scheme 3.3 also has the following mass conservation property.

Theorem 3.4. *The scheme* 3.3 *preserves the total mass, in the discrete sense that*

$$\int_\Omega \phi^n d\Omega = \int_\Omega \phi^0 d\Omega, \quad \forall n \geq 1. \tag{3.24}$$

Proof. Taking the inner product of (3.21a) with 1 over the domain Ω, we have

$$\int_\Omega \frac{\phi^1-\phi^0}{\Delta t} d\Omega = -M\alpha \int_\Omega (\phi^1-\overline{\phi}) d\Omega, \quad \overline{\phi} = \frac{1}{|\Omega|}\int_\Omega \phi^0 d\Omega, \tag{3.25}$$

which gives us

$$\Big(\frac{1}{\Delta t}+M\alpha\Big)\int_\Omega \phi^1 d\Omega = \Big(\frac{1}{\Delta t}+M\alpha\Big)\int_\Omega \phi^0 d\Omega. \tag{3.26}$$

Given the fact $M\alpha > 0$, we have $\int_\Omega \phi^1 d\Omega = \int_\Omega \phi^0 d\Omega$.

Next, assuming $\int_\Omega \phi^n d\Omega = \int_\Omega \phi^{n-1} d\Omega = \int_\Omega \phi^0 d\Omega$ with $n \geq 1$, we will show $\int_\Omega \phi^{n+1} d\Omega = \int_\Omega \phi^0 d\Omega$. Taking the inner product of (3.20a) with 1 over the domain Ω, we have

$$\int_\Omega \frac{(\theta+\frac{1}{2})\phi^{n+1}-2\theta\phi^n+(\theta-\frac{1}{2})\phi^{n-1}}{\Delta t} d\Omega = -M\alpha \int (\phi^{n+\theta}-\overline{\phi}) d\Omega. \tag{3.27}$$

There are two scenarios for the discretization of $\phi^{n+\theta}$. For the case in (3.2), we have

$$\begin{aligned}
&\Big[\frac{\theta+\frac{1}{2}}{\Delta t}+M\alpha(\theta+\beta\theta)\Big]\int_\Omega \phi^{n+1} d\Omega \\
=&\Big[\frac{2\theta}{\Delta t}-M\alpha(1-\theta-2\beta\theta)\Big]\int_\Omega \phi^n d\Omega + \Big[-\frac{\theta-\frac{1}{2}}{\Delta t}-M\alpha\beta\theta\Big]\int_\Omega \phi^{n-1} d\Omega + M\alpha\int_\Omega \phi^0 d\Omega \\
=&\Big[\frac{\theta+\frac{1}{2}}{\Delta t}+M\alpha(\theta+\beta\theta)\Big]\int_\Omega \phi^0 d\Omega.
\end{aligned} \tag{3.28}$$

Given the fact $\frac{\theta+\frac{1}{2}}{\Delta t}+M\alpha(\theta+\beta\theta) > 0$, we have $\int_\Omega \phi^{n+1} d\Omega = \int_\Omega \phi^0 d\Omega$. For the case in (3.3), we have

$$\begin{aligned}
&\Big[\frac{\theta+\frac{1}{2}}{\Delta t}+M\alpha\Big(\theta+\Big(\theta-\frac{1}{2}\Big)(1-\theta)\Big)\Big]\int_\Omega \phi^{n+1} d\Omega \\
=&\Big[\frac{2\theta}{\Delta t}-M\alpha\Big(1-\theta-2\Big(\theta-\frac{1}{2}\Big)(1-\theta)\Big)\Big]\int_\Omega \phi^n d\Omega \\
&+\Big[-\frac{\theta-\frac{1}{2}}{\Delta t}-M\alpha\Big(\theta-\frac{1}{2}\Big)(1-\theta)\Big]\int_\Omega \phi^{n-1} d\Omega + M\alpha\int_\Omega \phi^0 d\Omega \\
=&\Big[\frac{\theta+\frac{1}{2}}{\Delta t}+M\alpha\Big(\theta+\Big(\theta-\frac{1}{2}\Big)(1-\theta)\Big)\Big]\int_\Omega \phi^0 d\Omega.
\end{aligned} \tag{3.29}$$

Given the fact $\frac{1}{2} \leq \theta \leq \frac{3}{2}$, we have $\big[\frac{\theta+\frac{1}{2}}{\Delta t}+M\alpha(\theta+(\theta-\frac{1}{2})(1-\theta))\big] > 0$, we have $\int_\Omega \phi^{n+1} d\Omega = \int_\Omega \phi^0 d\Omega$.

Therefore, it holds $\int_\Omega \phi^n d\Omega = \int_\Omega \phi^0 d\Omega$, $\forall n \geq 1$. This completes the proof. □

3.2.3 Numerical approximations for molecular beam epitaxy model with slope selection

In a similar manner, we can obtain the numerical schemes for the MBE model in (2.22). The numerical scheme is given below.

Scheme 3.4. *Assuming that* (ϕ^n,q^n), *and* (ϕ^{n-1},q^{n-1}) *are already calculated with* $n\geq 1$, *we then compute* (ϕ^{n+1},q^{n+1}) *from the following temporal discrete system:*

$$\begin{aligned}&\frac{(\theta+\frac{1}{2})\phi^{n+1}-2\theta\phi^n+(\theta-\frac{1}{2})\phi^{n-1}}{\Delta t}\\ =&M\Big(-\varepsilon^2\Delta^2\phi^{n+\theta}+\gamma\Delta\phi^{n+\theta}+\nabla\cdot(q^{n+\theta}\mathbf{G}(\nabla\overline{\phi}^{n+\theta}))\Big),\end{aligned}\tag{3.30a}$$

$$\begin{aligned}&\frac{(\theta+\frac{1}{2})q^{n+1}-2\theta q^n+(\theta-\frac{1}{2})q^{n-1}}{\Delta t}\\ =&\mathbf{G}(\nabla\overline{\phi}^{n+1})\cdot\nabla\frac{(\theta+\frac{1}{2})\phi^{n+1}-2\theta\phi^n+(\theta-\frac{1}{2})\phi^{n-1}}{\Delta t},\end{aligned}\tag{3.30b}$$

where $\overline{(\cdot)}^{n+\theta}=(1+\theta)(\cdot)^n-\theta(\cdot)^{n-1}$, $\mathbf{G}(\nabla\phi)=\sqrt{2}\nabla\phi$ *and* $(\cdot)^{n+\theta}$ *is defined in either* (3.2) *or* (3.3).

Remark 3.5. We can compute (ϕ^1,q^1) from the following first-order Euler scheme:

$$\frac{\phi^1-\phi^0}{\Delta t}=M\Big(-\varepsilon^2\Delta\phi^1+\gamma\Delta\phi^1+\nabla\cdot(q^1\mathbf{G}(\nabla\phi^0))\Big),\tag{3.31a}$$

$$\frac{q^1-q^0}{\Delta t}=\mathbf{G}(\nabla\phi^0)\cdot\nabla\frac{\phi^1-\phi^0}{\Delta t}.\tag{3.31b}$$

Then, we can easily show that the proposed scheme 3.4 is unconditionally energy stable and preserve the total mass. The details are omitted for brevity.

4 Numerical examples

In this section, we implement the proposed schemes and present some numerical examples to demonstrate their effectiveness. The theoretical results will be numerically verified. Also, given the two cases in (3.2) and (3.3) are similar with proper choices of θ, we only focus on the case in (3.3) in the numerical examples. Thus, the θ mentioned below is chosen for (3.3) unless mentioned specifically.

4.1 Numerical examples for the Cahn-Hilliard model

First of all, we test our proposed numerical scheme for solving a benchmark problem of the Cahn-Hilliard model, which is proposed in [10]. Consider the domain $\Omega=[0,2\pi]\times$

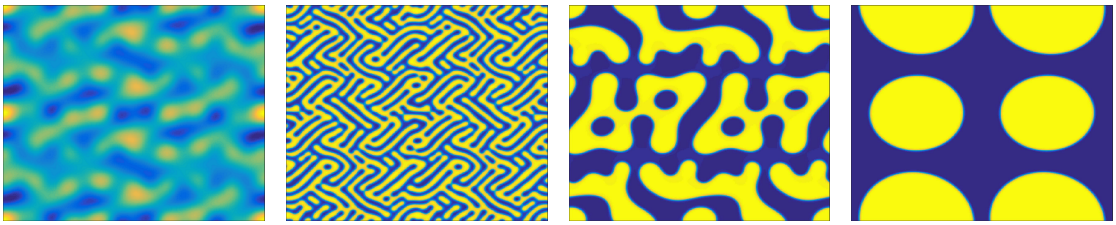

(a) ϕ at $t=0$ (b) ϕ at $t=0.05$ (c) ϕ at $t=2$ (d) ϕ at $t=150$

Figure 1: Time snapshots of coarsening dynamics driven by the Cahn-Hilliard model. The parameters used in these simulations are set as $M=1,\varepsilon=0.0199$ and $\theta=1.0$ in (3.3). The profiles of ϕ at different time slots are presented.

$[0,2\pi]$ with the model parameter $\varepsilon=0.0199$, $M=1$, and an initial condition

$$\phi|_{t=0}=0.05(\cos(3x)\cos(4y)+(\cos(4x)\cos(3y))^2+\cos(x-5y)\cos(2x-y)). \tag{4.1}$$

Take computational parameters $N=384$, $\theta=0.75$, $\delta t=10^{-4}$. The numerical results are summarized in Fig. 1, where we plot the time snapshots of coarsening dynamics driven by the Cahn-Hilliard model at time $t=0$, 0.05, 2, 150. Our numerical scheme provides accurate numerical solutions for the benchmark problem.

Also, to highlight the effectiveness of our proposed scheme, we compare it with the classical stabilized semi-implicit BDF scheme as below

$$\frac{3\phi^{n+1}-4\phi^n+\phi^{n-1}}{2\Delta t}=M\Delta\Big(-\varepsilon^2\Delta\phi^{n+1}+\gamma\phi^{n+1}+(\overline{\phi}^{n+1})^3-(1+\gamma)\overline{\phi}^{n+1}\Big). \tag{4.2}$$

In Fig. 2, we plot the time evolution of the energy for the Cahn-Hilliard model using the second-order scheme 3.2 and stabilized BDF scheme in (4.2) with $t\in[0,150]$ in log-log scale. In order to check the efficiency of the method, we also plot the reference energy by the solid red line. As shown in Fig. 2, the energy evolution for different methods is in good agreement when Δt is small enough. Fig. 2 indicates that our proposed scheme has compatible accuracy with the stabilized BDF scheme, but our proposed methods also automatically guarantee energy stability. We also emphasize that the semi-implicit BDF scheme without stabilizer, i.e., $\gamma=0$, shows poor stability (the gray line is the time evolution of energy with $\gamma=0,\delta t=0.0001$, while it will blow up with $\delta t=0.001,0.01$). Thus, we didn't use it for comparison purposes.

In the second example, we perform numerical simulations of coarsening dynamics in the domain $\Omega=[0,4\pi]\times[0,4\pi]$. The parameters are chosen as $M=0.02,\varepsilon=0.05$, and we use time step $\Delta t=10^{-3}$. The initial condition for ϕ is $\phi(t=0)=\text{rand}(-0.001,0.001)+\hat{\phi}_0$, where $\text{rand}(-0.001,0.001)$ be a random state by assigning a random number varying from -0.001 to 0.001 on each grid points and $\hat{\phi}_0$ be a constant. Here we choose the case in (3.3), and study the Δt_c for various θ. As shown in Table 1, we list Δt_c with $\gamma=0$ and different θ for the CH equation using the second order scheme 3.2.

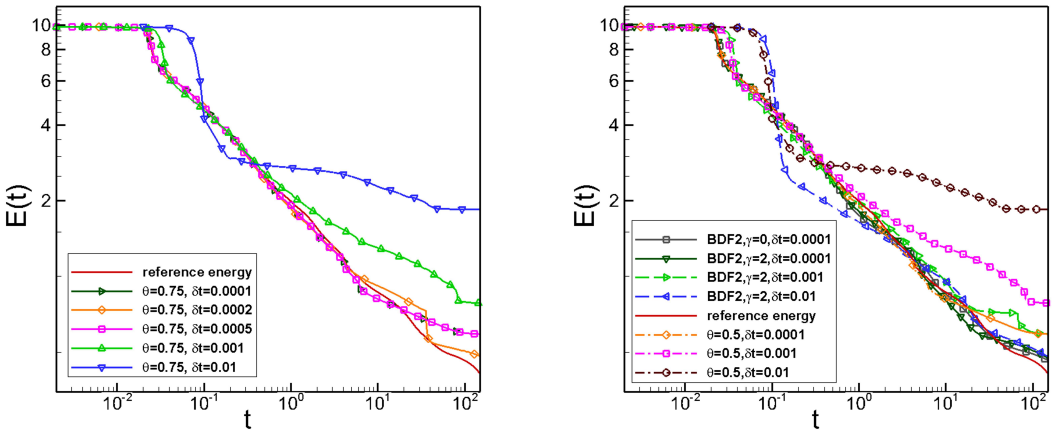

(a) (b)

Figure 2: Time evolution of the energy for the CH model. (a) results using the second order scheme 3.2; and (b) results using the second order scheme 3.2 and the BDF2 scheme in (4.2). The numerical energies with $t\in[0,150]$ in log-log scale are shown. The red solid line is the reference energy. The parameters are set as $\Delta t=10^{-4},2\times10^{-4},5\times10^{-4},10^{-3},10^{-2}$, $\gamma=2$ and $\theta=0.5,0.75$.

Table 1: Δt_c with $\gamma=0$ and different θ for the CH equation using second order scheme 3.2.

θ	0.5	0.75	1.0	1.25	1.5
Δt_c	(0.24,0.25)	(0.18,0.19)	(0.18,0.19)	(0.2,0.21)	(0.24,0.25)

Then, we study how the initial profile would affect the coarsening dynamics. We choose $\phi|_{t=0}=\hat{\phi}_0+\text{rand}(-0.001,0.001)$, with c_0 a constant. The profiles of ϕ with various $\hat{\phi}_0$ at different time slots are summarized in Fig. 3. As it is shown in Fig. 3, phase separation dynamics are observed, which is a good indicator of the numerical scheme producing durable numerical results. Also, we observe that spinodal decomposition dynamics are dominant when $\hat{\phi}_0=0$, and nucleation dynamics are dominant when $\hat{\phi}_0=0.4$.

In Fig. 4, we plot the time evolution of the energy for the Cahn-Hilliard model using the second order scheme 3.2 with $t\in[0,150]$ in log-log scale. The time step is set at $\Delta t=10^{-3}$, along with the parameters $\gamma=0$ and $\theta=0.5,0.75,1.0,1.25,1.5$ for the case in (3.3). As shown in Fig. 4, the energy evolution for different θ are in good agreement, i.e. the schemes with different θ all guarantee accurate results.

In Fig. 5, the time evolution of the energy for the Cahn-Hilliard model is plotted using the second order scheme 3.2 with $t\in[0,150]$ in log-log scale. The time step is set at $\Delta t=10^{-4},10^{-3},10^{-2},10^{-1}$, along with the parameters $\gamma=0$ and $\theta=0.75$ for the case in (3.3). The energy evolution for different Δt are in good agreement as shown in Fig. 5.

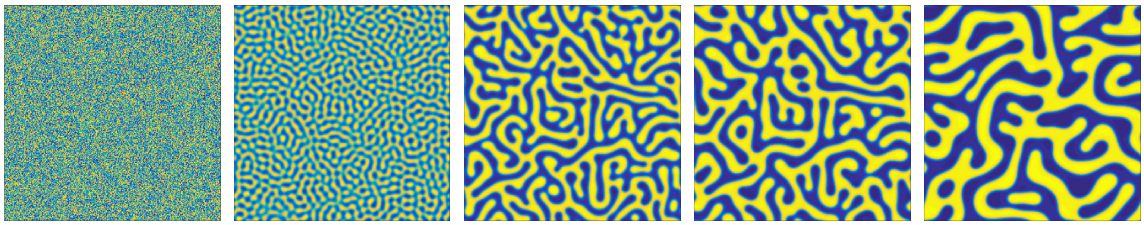

(a) ϕ at $t=0,5,25,50,150$ with $\hat{\phi}_0=0$

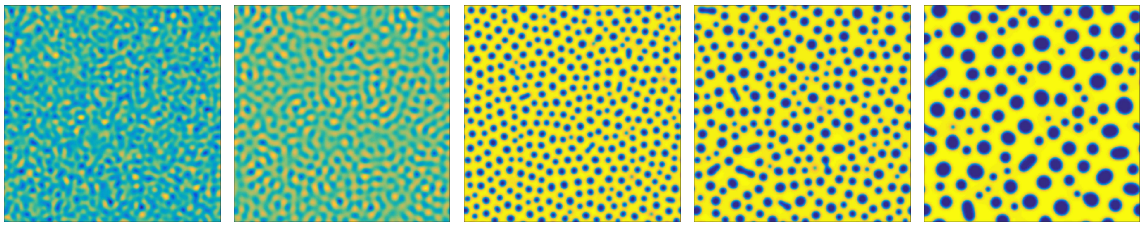

(b) ϕ at $t=1,10,20,50,150$ with $\hat{\phi}_0=0.4$

Figure 3: Time snapshots of coarsening dynamics driven by the Cahn-Hilliard model with various initial conditions. The parameters used in these simulations are set as $M=0.02,\varepsilon=0.05$ and $\theta=0.5$ in (3.3). The profiles of ϕ at different time slots are presented.

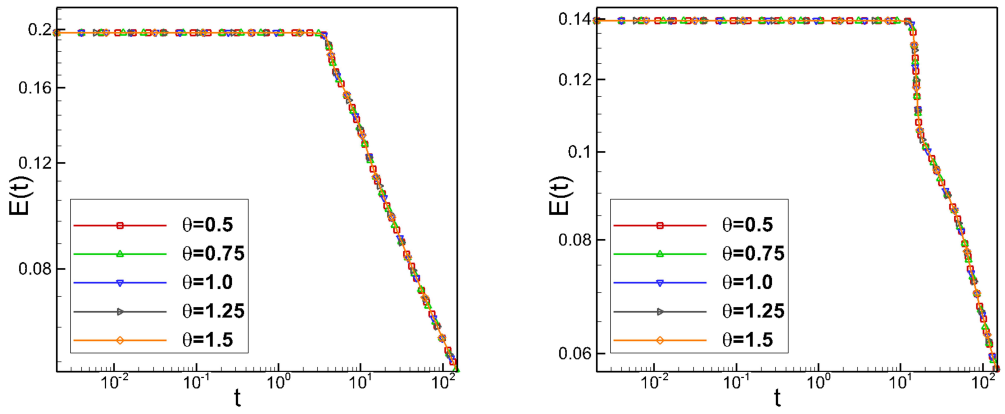

(a) (b)

Figure 4: Time evolution of the energy for the CH model with various initial conditions. (a) $\phi(t=0)=$ rand$(-0.001,0.001)$ and (b) $\phi(t=0)=$ rand$(-0.001,0.001)+0.4$. We use the second order scheme 3.2, and the results for $t\in[0,150]$ in log-log scale are shown. The parameters are set as $\Delta t=10^{-3}$, $\gamma=0$ and $\theta=0.5,0.75,1.0,1.25,1.5$.

4.2 Numerical examples for the diblock-copolymer model

In this subsection, we implement the scheme 3.3 to investigate the diblock-copolymer model in (2.16). Several numerical tests are summarized. First of all, we use the domain $\Omega=[0,4\pi]^2$, $M=0.02$, $\varepsilon=0.05$, and nonlocal parameter $\alpha=5$. We choose $\theta=0.5$ for the

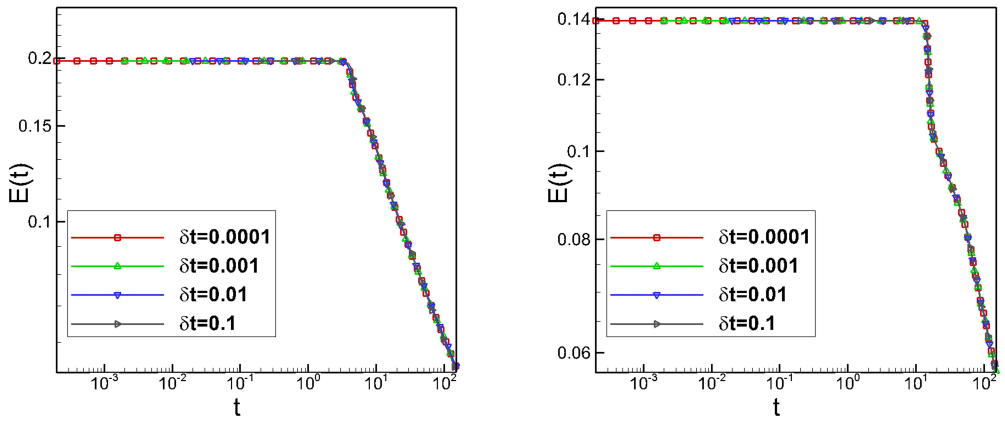

Figure 5: Time evolution of the energy for the CH model with different initial conditions. (a) $\phi(t=0)=$ rand$(-0.001,0.001)$, and (b) $\phi(t=0)=$rand$(-0.001,0.001)+0.4$. We use the second order scheme 3.2. The results with $t\in[0,150]$ in log-log scale are shown. The parameters are set as $\Delta t=10^{-4},10^{-3},10^{-2},10^{-1}$, $\gamma=0$ and $\theta=0.75$.

case in (3.3), $\gamma=0$, and set the initial condition

$$\phi|_{t=0}=c_0+\text{rand}(-0.001,0.001), \tag{4.3}$$

with c_0 a constant. The effects of initial condition on the coarsening dynamics are investigated. We choose $c_0=0$ and 0.4. With $\Delta t=10^{-3}$, the numerical profiles of ϕ and $t=1,5,10,20,150$ for both cases are summarized in Fig. 6. We observe that the phase separation dynamics is similar to the Cahn-Hilliard model, but the final phase present different pattern. The equilibrium is much faster than the numerical result obtained by the Cahn-Hilliard model.

In Fig. 7, the time evolution of the energy for the phase-field diblock copolymer model using the second-order scheme 3.3 with $t\in[0,150]$ in log-log scale is plotted. It indicates the scheme performs well with various choices of θ.

The time evolution of the energy for the phase-field diblock copolymer model using the second-order scheme 3.3 with $t\in[0,150]$ in log-log scale is plotted in Fig. 8. Similar to the above example, the scheme performs well with various Δt.

Next, we investigate the effect of nonlocal parameter α on the bubble assemble dynamics. In this case, we set the domain $\Omega=[0,4\pi]^2$, and the model parameters $M=1$, $\varepsilon=0.06$. The initial profile is chosen as $\phi|_{t=0}=$rand$(-0.005,0.005)+0.4$. For the numerical parameters, we chose $\Delta t=0.001$, $\theta=0.5$ for the case in (3.3), and we calculate the solution to $t=100$. The profiles for ϕ at $t=100$ are summarized in Fig. 9. We observe that the bubbles have roughly the same radius in each case, and the radius decreases as α increases. As the total volume of the bubbles is conserved, it also means, as α increases, the number of bubbles in the assemblies grows accordingly.

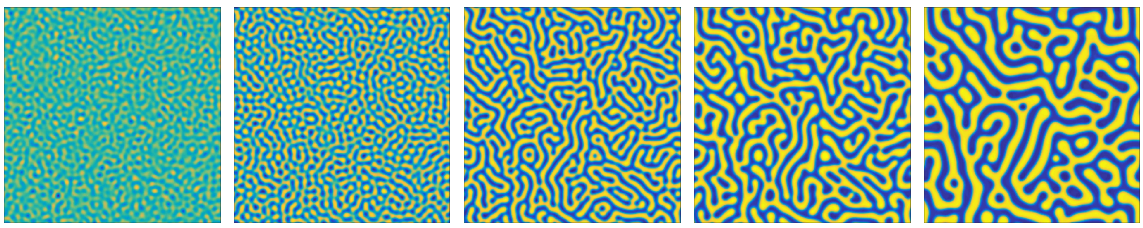

(a) ϕ at $t=1,5,20,20,150$ with $c_0=0$

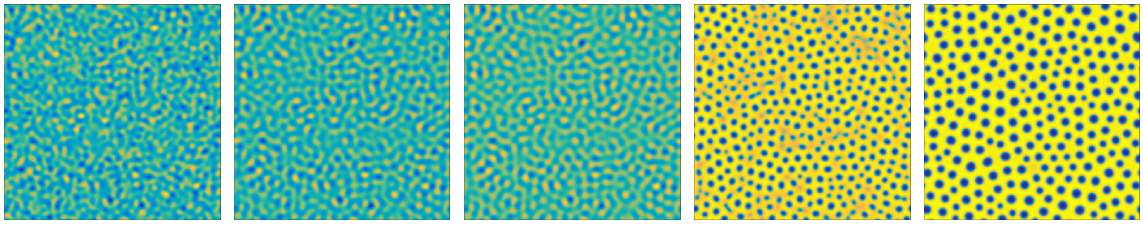

(b) ϕ at $t=1,5,20,20,150$ with $c_0=0.4$

Figure 6: Time snapshots of coarsening dynamics driven by the phase field diblock copolymer model with various initial conditions. The parameters are set as $M=0.02,\varepsilon=0.05$, $\theta=0.5$ and $\gamma=0$. The profiles of ϕ at different time slots $t=1,5,10,20,40,150$ are presented.

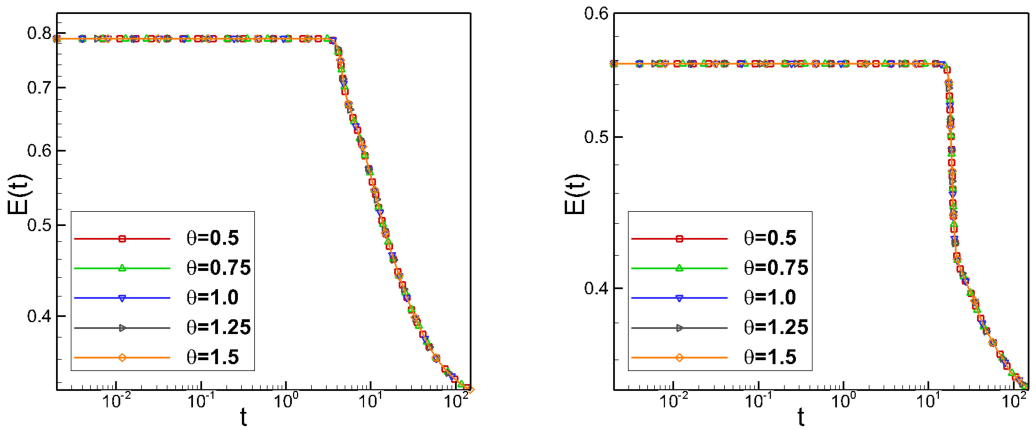

(a) (b)

Figure 7: Time evolution of the energy for the phase field diblock copolymer model with various initial conditions. In (a), we use $\phi(t=0)=\text{rand}(-0.001,0.001)$, and we use $\phi(t=0)=\text{rand}(-0.001,0.001)+0.4$ in (b). The results using the second order scheme 3.3 with $t\in[0,150]$ in log-log scale are presented. The parameters are set as $\Delta t=10^{-3}$, $\gamma=0$ and $\theta=0.5,0.75,1.0,1.25,1.5$ for the case in Eq. (3.3).

To better understand the scaling relations between bubble numbers and the nonlocal interaction parameter α, we present a log-log plot of the number of the droplets versus α in Fig. 10. For $\alpha=0.125,0.4,1,2.25,3.6$, the corresponding number of double bubbles are $K_\alpha=4,9,15,25,34$, respectively. The line $K_\alpha\propto\alpha^{2/3}$ is also plotted for reference. From

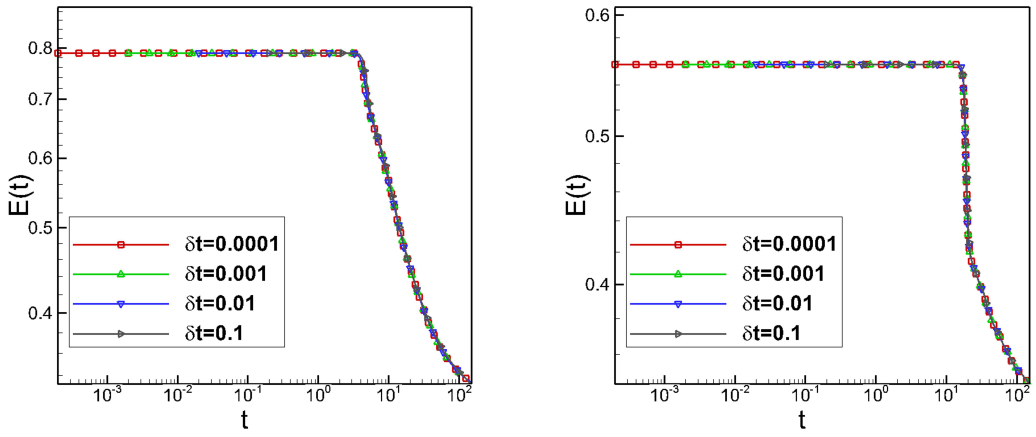

(a) (b)

Figure 8: Time evolution of the energy for the phase field diblock copolymer model two different initial conditions: (a) $\phi(t=0)=\text{rand}(-0.001,0.001)$ (left) and (b) $\phi(t=0)=\text{rand}(-0.001,0.001)+0.4$. With the second order scheme 3.3, the calculated results for $t\in[0,150]$ in log-log scale are presented. The parameters are set as $\Delta t=10^{-4},10^{-3},10^{-2},10^{-1}$, $\gamma=0$ and $\theta=0.75$ for the case in Eq. (3.3).

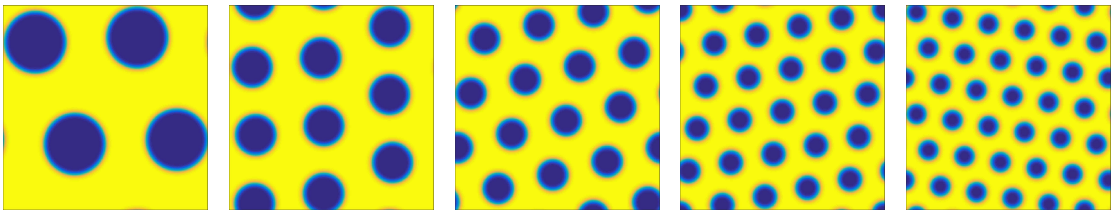

(a) $\alpha=0.125$ (b) $\alpha=0.4$ (c) $\alpha=1$ (d) $\alpha=2.25$ (e) $\alpha=3.6$

Figure 9: Steady state of the bubble assembles driven by the phase field diblock copolymer model. Here we choose the initial condition $\phi|_{t=0}=\text{rand}(-0.005,0.005)+0.4$ on domain $[-\pi,\pi]\times[-\pi,\pi]$. The parameters are set as $M=1,\varepsilon=0.06$ and $\theta=0.5$. The profiles of ϕ with different α at time $t=100$ are presented.

Fig. 10, we observe that the number of bubbles scales approximately as $K_\alpha\propto\alpha^{2/3}$. This phenomenon agrees with the theoretical studies [39] and numerical results [51].

4.3 Numerical examples for the MBE model

In the last case, we consider the MBE model (2.22) with the initial condition as following:

$$\phi(x,y,t=0)=0.1(\sin 3x\sin 2y+\sin 5x\sin 5y). \tag{4.4}$$

We take the computational domain as $\Omega=[0,2\pi]^2$ and discretize the space with 128×128 uniform grid points by the Fourier spectral method. And we define the roughness

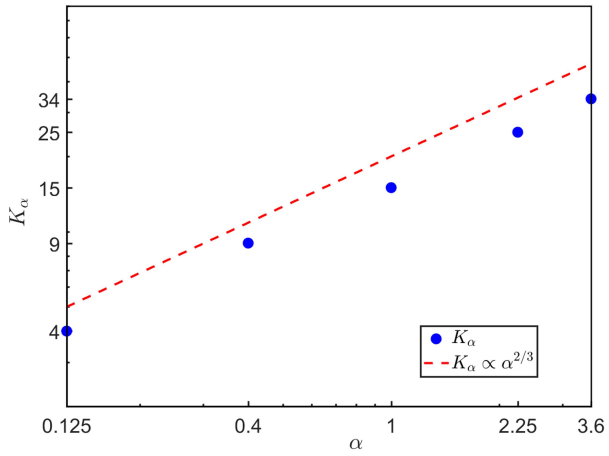

Figure 10: Log-log plot of the dependence of the number of bubbles on α in the bubble assemblies. As α increases, the number of bubbles in the assemblies grows accordingly. For $\alpha = 0.125,0.4,1,2.25,3.6$, the corresponding number of double bubbles are $K_\alpha = 4,9,15,25,34$, respectively, which indicates that the number of bubbles obeys a scaling law $K_\alpha \propto \alpha^{2/3}$ approximately.

measure function $W(t)$ as

$$W(t) = \sqrt{\frac{1}{|\Omega|}\int_\Omega \Big(\phi(x,y,t) - \overline{\phi}(x,y,t)\Big)^2 d\Omega},$$

where $\overline{\phi}(x,y,t) = \int_\Omega \phi(x,y,t) d\Omega$.

We begin with the numerical test of the time accuracy for the second-order scheme (3.4). Since the exact solution for MBE growth model is unknown, we use numerical results of scheme (3.4) with $\gamma = 0, \Delta t = 0.00001$ and $N = 128$ as the exact solution. Taking $\varepsilon = 1$ and the numerical errors are computed at $T = 1$.

In Fig. 11, the error versus time step Δt for the MBE growth model are shown using the second order scheme 3.4 with different regularization parameter $\gamma = 0.0$ (left) and $\gamma = 4.0$ (right) and various parameter $\theta = 0.5,0.75,1.0,1.25,1.5$ for the case in (3.3). With different regularization parameter $\gamma = 0,4$, the expected second order convergence rate in time is obtained. From this figures, we can conclude that the error decreasing as θ increasing.

In addition, we show the time evolution of the energy and rough for the MBE growth model using the second order scheme 3.4 when $t \in [0,30]$ (left) and $t \in [5,11]$ (right) in Fig. 12. We set the time step as $\Delta t = 10^{-3}, 10^{-4}$ and $\gamma = 0$ and various parameter θ. From Fig. 12, we observe the energy evolution is more closer to the exact one with time step $\Delta t = 10^{-3}$ as θ decreasing.

Also, we present the time evolution of the energy (left) and rough (right) for the MBE growth model using the second order scheme 3.4 when $t \in [0,30]$ with $\theta = 0.5$ and $\theta = 1.5$

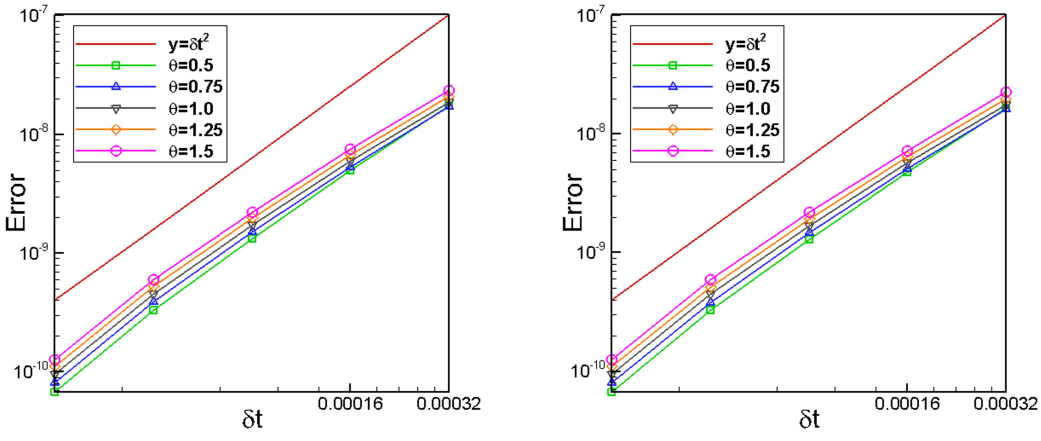

(a) $\gamma=0$ (b) $\gamma=4$

Figure 11: Time accuracy convergence test. In the figures, the error versus time step Δt for the MBE growth model are shown using second order scheme 3.4 with different regularization parameters with $\varepsilon^2=1$ and various parameter $\theta=0.5,0.75,1.0,1.25,1.5$.

in Fig. 13. In this simulation, we set the time step at $\Delta t=10^{-3},10^{-4}$ and $\gamma=0,10,20$. And, we enlarge the time evolution of the energy and rough with different time steps and γ at time region $[5,11]$ in inset figures. From Fig. 13, we observe the energy and rough evolution are consistent with the exact one with time step $\Delta t=10^{-4}$, and $\Delta t=10^{-3}$ by adding regularization parameter $\gamma=20.0$. But the results with $\Delta t=10^{-3}$ by adding regularization parameter $\gamma=0.0$ and $\gamma=10.0$ is not accurate enough.

We plot the time evolution of the energy (left) and rough (right) for the MBE growth model using the second order scheme 3.4 when $t\in[0,30]$ in Fig. 14. The time step is set at $\Delta t=10^{-4}$. And we set $\gamma=0$ and $\theta=0.5,0.75,1.0,1.25,1.5$. It demonstrates that the evolution of the MBE growth model is accuracy when Δt is small enough for various θ.

In this example, we perform numerical simulations of coarsening dynamics in the domain $[0,12.8]\times[0,12.8]$. The initial condition is a random state by assigning a random number, which varies from -0.001 to 0.001 to each grid point. The numerical schemes we have proposed are unconditionally stable, but the global error accumulated in time evolution will lead to the wrong solution, especially with the non-smooth initial condition. Define Δt_c as the largest possible time step, which allows stable numerical computation. In Table 2, we list the values of Δt_c for the MBE growth model using second-order scheme 3.4 with regularization parameter $\gamma=0$. The the semi-discrete scheme is approximated by the Fourier spectral methods in space with Fourier mode number $N=512$. Table 2 demonstrates that different stability for different parameter θ.

We plot the time evolution of the energy (left) and rough (right) for the MBE growth model using the second-order scheme 3.4 when $t\in[0.1,100]$ in Fig. 15. The power-law scaling dynamics are observed, which agrees well with other published results [46]. This

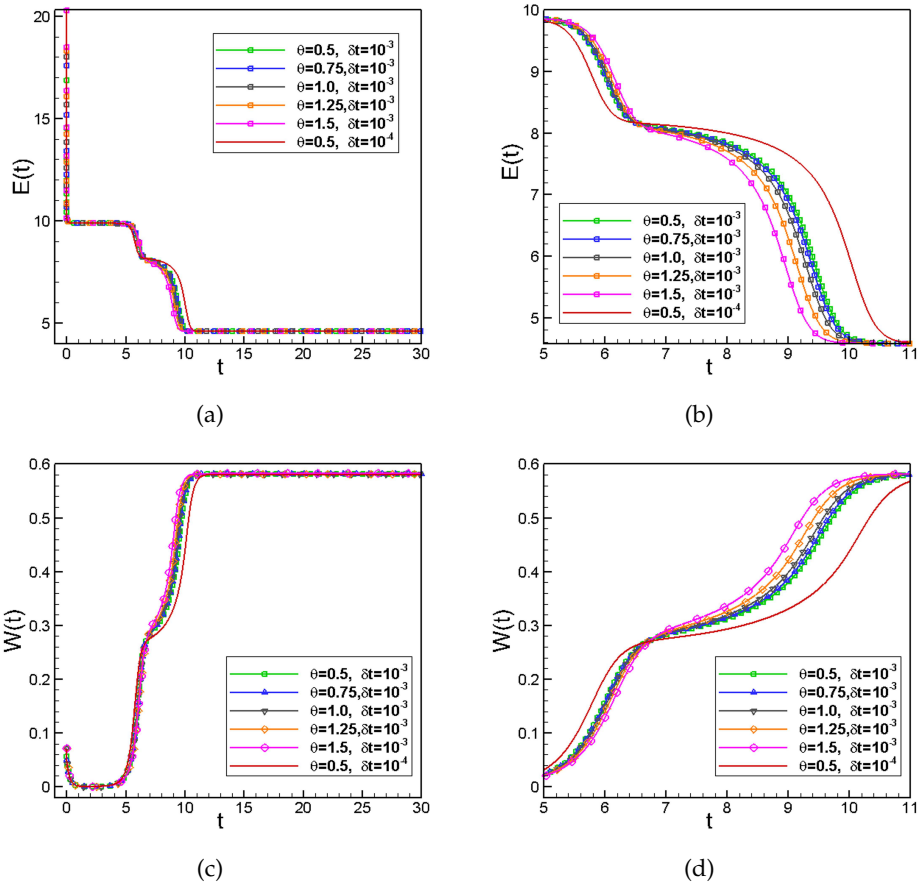

Figure 12: Time evolution of the energy for the MBE growth model using second order scheme 3.4. (a) Energy evolution for $t\in[0,30]$; (b) zoomed energy evolution for $t\in[5,11]$; (c) roughness evolution for $t\in[0,30]$; and (d) zoomed roughness evolution for $t\in[5,11]$. The time step is set at $\Delta t=10^{-3},10^{-4}$ and $\gamma=0$ and various parameter θ.

Table 2: Δt_c with $\gamma=0$ and different θ for the MBE growth model using second order scheme 3.4.

θ	0.5	0.75	1.0	1.25	1.5
Δt_c	(0.0005,0.0005)	(0.0012,0.0013)	(0.0012,0.0013)	(0.0012,0.0013)	(0.0007,0.0008)

illustrates the effectiveness of the proposed schemes. In particular, when the time step size is small enough, the evolution of the energy and rough are in agreement for various θ.

Here we use time step $\Delta t=0.001$. The parameters are chosen as $\gamma=0.0$ and $\theta=1.25$. The isolines of numerical solutions of the height function ϕ and its Laplacian $\Delta\phi$ for the MBE growth model with random initial conditions are plotted in Fig. 16, which is in substantial agreement with other published results [46].

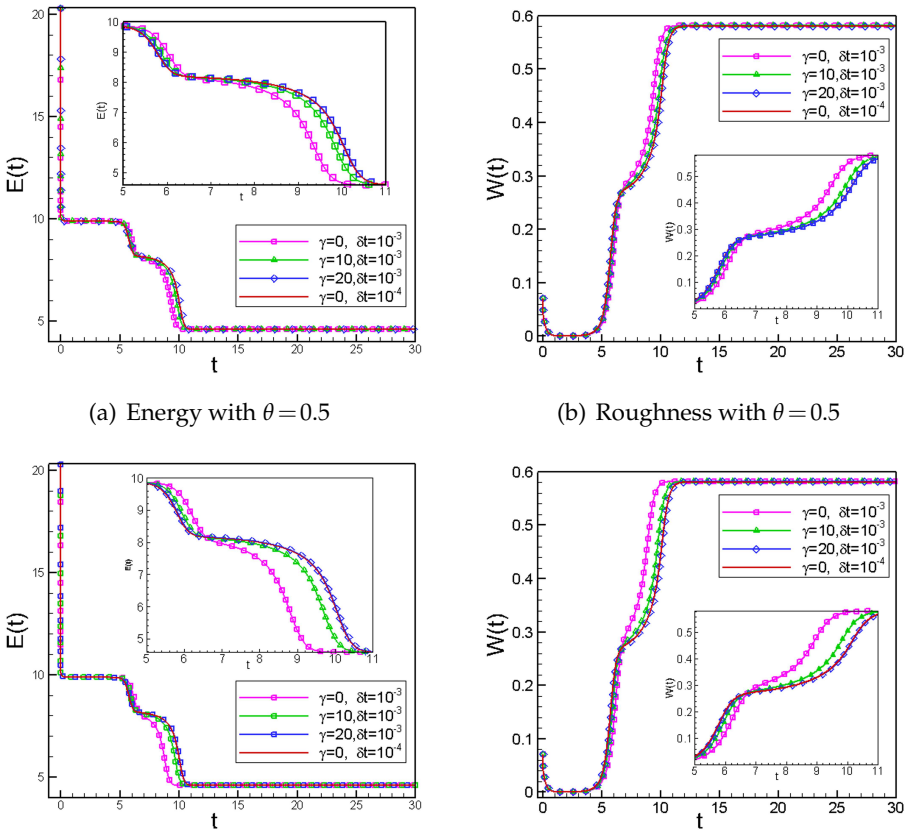

(a) Energy with $\theta=0.5$ (b) Roughness with $\theta=0.5$

(c) Energy with $\theta=1.5$ (d) Roughness with $\theta=1.5$

Figure 13: Time evolution of the energy and roughness for the MBE growth model using second order scheme 3.4 when $t\in[0,30]$ and $t\in[5,11]$ (inset figure). The time step is set at $\Delta t=10^{-3},10^{-4}$ and $\gamma=0,10,20$. (a) $\theta=0.5$; (b) $\theta=1.5$.

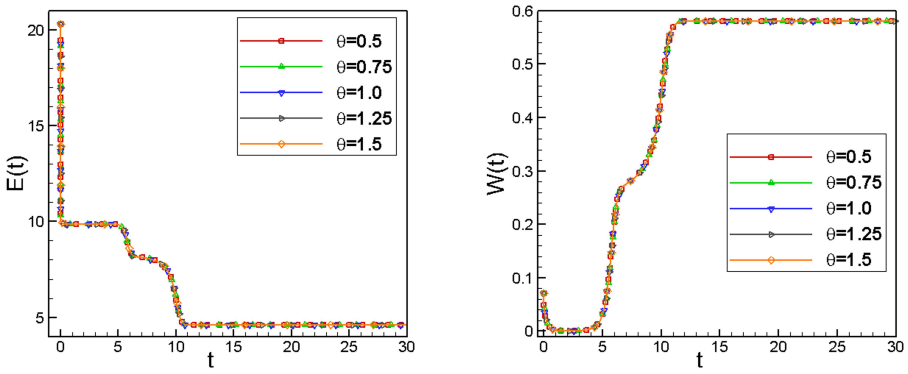

Figure 14: Time evolution of the energy (left) and rough (right) for the MBE growth model using the second order scheme 3.4 when $t\in[0,30]$. The time step is set at $\Delta t=10^{-4}$ and $\gamma=0$ and $\theta=0.5,0.75,1.0,1.25,1.5$.

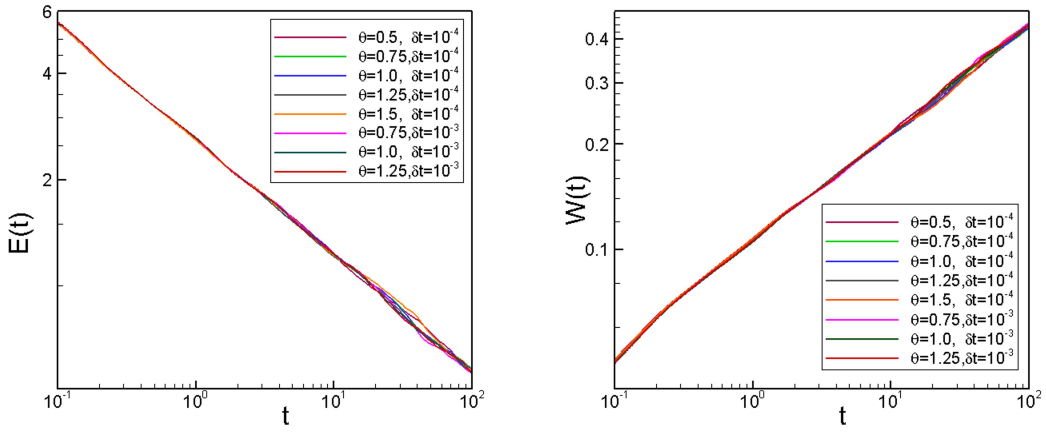

(a) Energy scaling law (b) Roughness scaling law

Figure 15: Time evolution of the energy and roughness for the MBE growth model using the second order scheme 3.4 when $t\in[0.1,100]$. The time step is set at $\Delta t=10^{-4}$ or 10^{-3} with $\gamma=0$ and $\theta=0.5,0.75,1.0,1.25,1.5$.

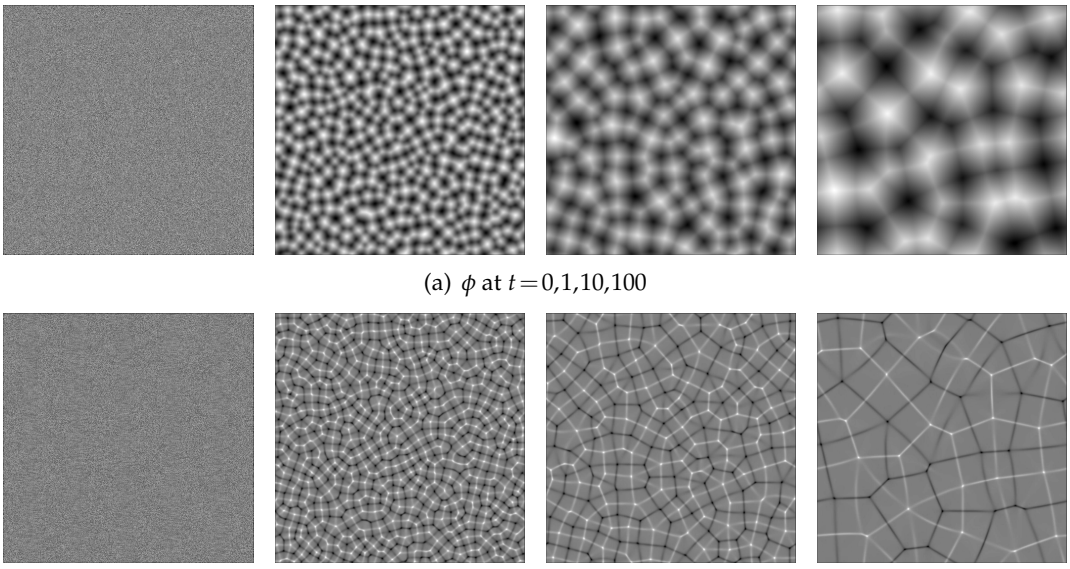

(a) ϕ at $t=0,1,10,100$

(b) $\Delta\phi$ at $t=0,1,10,100$

Figure 16: The isolines of numerical solutions of the height function ϕ and its Laplacian $\Delta\phi$ for the MBE growth model with random initial condition. Snapshots for ϕ and $\Delta\phi$ are taken at $t=0,1,10,100$, respectively.

5 Conclusion

In this paper, we propose a new family of second-order numerical schemes for approximating phase field models. This new family of numerical schemes improves the invariant

energy quadratization (IEQ) method by introducing extra free parameters, which could be further tuned to improve the numerical schemes' stability and accuracy. In addition, the newly proposed scheme is linear, second-order accuracy in time, and unconditionally energy stable. Convergence tests and several numerical examples are shown to verify the effectiveness of the proposed schemes. Some explorations on the optimal choices of the free parameters are conducted. We apply this new class of numerical algorithms to the Cahn-Hilliard model, the diblock copolymer model, and the MBE model for illustration purposes. The newly proposed schemes are rather general and apply widely to thermodynamically consistent phase field models in the literature.

Acknowledgments

Lizhen Chen would like to acknowledge the support from the National Natural Science Foundation of China Grants U1930402. Zengyan Zhang and Jia Zhao would like to acknowledge the support from the National Science Foundation of USA with grant DMS-1816783.

References

[1] S. Badia, F. Guillén-González, and J. V. Gutiérrez-Santacreu. Finite element approximation of nematic liquid crystal flows using a saddle-point structure. *Journal of Computational Physics*, 230(4):1686–1706, 2011.

[2] J. W. Cahn and J. E. Hilliard. Free energy of a nonuniform system. I. Interfacial free energy. *Journal of Chemical Physics*, 28:258–267, 1958.

[3] J. W. Cahn and J. E. Hilliard. Free energy of a nonuniform system. I. Interfatial free energy. *Journal of Chemical Physics*, 28(2), February 1958.

[4] L. Chen, J. Zhao, and Y. Gong. A novel second-order scheme for the molecular beam epitaxy model with slope selection. *Commun. Comput. Phys*, 25(4):1024–1044, 2019.

[5] L. Chen, J. Zhao, and X. Yang. Regularized linear schemes for the molecular beam epitaxy model with slope selection. *Applied Numerical Mathematics*, 128:138–156, 2018.

[6] R. Chen, G. Ji, X. Yang, and H. Zhang. Decoupled energy stable schemes for phase-field vesicle membrane model. *Journal of Computational Physics*, 302:509–523, 2015.

[7] W. Chen, C. Wang, X. Wang, and S. Wise. Positivity-preserving, energy stable numerical schemes for the Cahn-Hilliard equation with logarithmic potential. *Journal of Computational Physics*, X(3):100031, 2019.

[8] K.L. Cheng, C. Wang, and S. M. Wise. An energy stable bdf2 fourier pseudo-spectral numerical scheme for the square phase field crystal equation. *Commun. Comput. Phys.*, 26:1335–1364, 2019.

[9] R. Choksi, M. A. Peletier, and J. F. Williams. On the phase diagram for microphase separation of diblock copolymers: An approach via a nonlocal Cahn-Hilliard functional. *SIAM J. Appl. Math.*, 69(6):1712–1738, 2009.

[10] J.M. Church, Z.L. Guo, P.K. Jimack, A. Madzvamuse, K. Promislow, B. Wetton, S. M. Wise, and F.W. Yang. High accuracy benchmark problems for Allen-Cahn and Cahn-Hilliard dynamics. *Commun. Comput. Phys.*, 26:947–972, 2019.

[11] M Dahlby and B Owren. A general framework for deriving integral preserving numerical methods for PDEs. *SIAM Journal of Scientific Computing*, 33(5):2318–2340, 2011.

[12] A. Diegel, C. Wang, X. Wang, and S. Wise. Convergence analysis and error estimates for a second order accurate finite element method for the Cahn-Hilliard-Navier-Stokes system. *Numerische Mathematic*, 137:495–534, 2017.

[13] S. Dong, Z. Yang, and L. Lin. A family of second-order energy-stable schemes for Cahn-Hilliard type equations. *Journal of Computational Physics*, 383:24–54, 2019.

[14] Q. Du, L. Ju, X. Li, and Z. Qiao. Maximum principle preserving exponential time differencing schemes for the nonlocal Allen-Cahn equation. *SIAM Journal on Numerical Analysis*, 57(2):875–898, 2019.

[15] K. R. Elder and M. Grant. Modeling elastic and plastic deformations in nonequilibrium processing using phase field crystals. *Physical Review E*, 70(051605), 2004.

[16] K. R. Elder, M. Katakowski, M. Haataja, and M. Grant. Modeling elasticity in crystal growth. *Physical Review Letters*, 88(245701), 2002.

[17] C. M. Elliott and A. M. Stuart. The global dynamics of discrete semilinear parabolic equations. *SIAM Journal on Numerical Analysis*, 30(6):1622–1663, 1993.

[18] D. Eyre. Unconditionally gradient stable time marching the Cahn-Hilliard equation. *Computational and mathematical models of microstructural evolution (San Francisco, CA, 1998)*, 529:39–46, 1998.

[19] K. Glasner and S. Orizaga. Improving the accuracy of convexity splitting methods for gradient flow equations. *Journal of Computational Physics*, 315:52–64, 2016.

[20] Y. Gong and J. Zhao. Energy-stable rungekutta schemes for gradient flow models using the energy quadratization approach. *Applied Mathematics Letters*, 94:224–231, 2019.

[21] Y. Gong, J. Zhao, and Q. Wang. Arbitrarily high-order linear energy stable schemes for gradient flow models. *Journal of Computational Physics*, 419:109610, 2020.

[22] Y. Gong, J. Zhao, and Q. Wang. Arbitrarily high-order unconditionally energy stable schemes for thermodynamically consistent gradient flow models. *SIAM Journal on Scientific Computing*, 42(1):B135–B156, 2020.

[23] Z. Guan, J. Lowengrub, C. Wang, and S. Wise. Second order convex splitting schemes for periodic nonlocal Cahn-Hilliard and Allen-Cahn equations. *Journal of Computational Physics*, 277:48–71, 2014.

[24] F. Guillén-González and G. Tierra. On linear schemes for a Cahn-Hilliard diffuse interface model. *Journal of Computational Physics*, 234:140–171, 2013.

[25] F. Guillen-Gonzalez and G. Tierra. Second order schemes and time-step adaptivity for Allen-Cahn and Cahn-Hilliard models. *Computers and Mathematics with Applications*, 68:821–846, 2014.

[26] J. Guo, C. Wang, S. Wise, and X. Yue. An H^2 convergence of a second-order convex-splitting, finite difference scheme for the three-dimensional Cahn-Hilliard equation. *Commun. Math. Sci.*, 14(2):489–515, 2015.

[27] Z. Hu, S. M. Wise, C. Wang, and J. S. Lowengrub. Stable and efficient finite difference nonlinear-multigrid schemes for the phase field crystal equation. *J. Comput. Phys.*, 228:5323–5339, 2009.

[28] M. Jiang, Z. Zhang, and J. Zhao. Improving the accuracy and consistency of the scalar auxiliary variable (SAV) method with relaxation. *arXiv*, page 2104.06620, 2021.

[29] N. Jiang, M. Mohebujjaman, L. Rebholz, and C. Trenchea. An optimally accurate discrete regularization for second order timestepping methods for Navier-Stokes equations. *Computer Methods in Applied Mechanics and Engineering*, 310:388–405, 2016.

[30] L. Ju, X. Li, Z. Qiao, and H. Zhang. Energy stability and error estimates of exponential time differencing schemes for the epitaxial growth model without slope selection. *Mathematics of Computation*, 87:1859–1885, 2018.
[31] J. Kim, K. Kang, and J. Lowengrub. Conservative multigrid methods for ternary Cahn-Hilliard systems. *Commun. Math. Sci.*, 2:53–77, 2004.
[32] D. Li and Z. Qiao. On second order semi-implicit Fourier spectral methods for 2D Cahn-Hilliard equations. *Journal of scientific computing*, 70(1):301–341, 2017.
[33] D. Li, Z. Qiao, and T. Tang. Characterizing the stabilization size for semi-implicit Fourier-spectral method to phase field equations. *SIAM Journal on Numerical Analysis*, 54(3):1653–1681, 2016.
[34] X. Li, L.L. Ju, and X.C. Meng. Convergence analysis of exponential time differencing schemes for the Cahn-Hilliard equation. *Commun. Comput. Phys.*, 26:1510–1529, 2019.
[35] Y. Li, J. Kim, and N. Wang. An unconditionally energy-stable second-order time-accurate scheme for the Cahn-Hilliard equation on surfaces. *Commun Nonlinear Sci Numer Simulat*, 53:213–227, 2017.
[36] C. Liu, J. Shen, and X. Yang. Dynamics of defect motion in nematic liquid crystal flow: modeling and numerical simulation. *Comm. Comput. Phys*, 2:1184–1198, 2007.
[37] L. Onsager. Reciprocal relations in irreversible processes I. *Physical Review*, 37:405–426, 1931.
[38] L. Onsager. Reciprocal relations in irreversible processes II. *Physical Review*, 38:2265–2279, 1931.
[39] X. Ren and J. Wei. Many droplet pattern in the cylindrical phase of diblock copolymer morphology. *Rev. Math. Phys.*, 19(8):879–921, 2007.
[40] J. Shen, C. Wang, X. Wang, and S. M. Wise. Second-order convex splitting schemes for gradient flows with Ehrlich-Schwoebel type energy: Application to thin film epitaxy. *SIAM Journal on Numerical Analysis*, 50(1):105–125, 2012.
[41] J. Shen, J. Xu, and J. Yang. A new class of efficient and robust energy stable schemes for gradient flows. *SIAM Review*, 61(3):474–506, 2019.
[42] J. Shen, J. Xu, and J. Yang. The scalar auxiliary variable (SAV) approach for gradient flows. *Journal of Computational Physics*, 353:407–416, 2018.
[43] J. Shen and X. Yang. Numerical approximations of Allen-Cahn and Cahn-Hilliard equations. *Discrete and Continuous Dynamical Systems-Series A*, 28(4):1669–1691, 2010.
[44] J. Shen and X. Yang. A phase-field model for two-phase flows with large density ratio and its numerical approximation. *SIAM Journal of Scientific Computing*, 32:1159–1179, 2010.
[45] J. Shin, H. Lee, and J. Lee. Convex splitting Runge-Kutta methods for phase-field models. *Computers and Mathematics with Applications*, 73:2388–2403, 2017.
[46] C. Wang, X. Wang, and S. Wise. Unconditionally stable schemes for equations of thin film epitaxy. *Discrete and Continuous Dynamic Systems*, 28(1):405–423, 2010.
[47] C. Wang and S. M. Wise. An energy stable and convergent finite-difference scheme for the modified phase field crystal equation. *SIAM J. Numer. Anal.*, 49:945–969, 2011.
[48] S. Wise, C. Wang, and J. S. Lowengrub. An energy-stable and convergent finite-difference scheme for the phase field crystal equation. *SIAM Journal of Numerical Analysis*, 47(3):2269–2288, 2009.
[49] C. Xu and T. Tang. Stability analysis of large time-stepping methods for epitaxial growth models. *SIAM Journal on Numerical Analysis*, 44(4):1759–1779, 2006.
[50] J. Xu, Y. Li, S. Wu, and A. Bousquet. On the stability and accuracy of partially and fully implicit schemes for phase field modeling. *Computer Methods in Applied Mechanics and Engineering*, 345:826–853, 2019.

[51] X. Xu and Y. X. Zhao. Energy stable semi-implicit schemes for Allen-Cahn-Ohta-Kawasaki model in binary system. *J. Sci. Comput.*, 80:1656–1680, 2019.
[52] X. Yang, G. Forest, C. Liu, and J. Shen. Shear cell rupture of nematic liquid crystal droplets in viscous fluids. *Journal of Non-Newtonian Fluid Dynamics*, 166:487–499, 2011.
[53] X. Yang, J. Li, G. Forest, and Q. Wang. Hydrodynamic theories for flows of active liquid crystals and the generalized onsager principle. *Entropy*, 18(6):202, 2016.
[54] X. Yang, J. Zhao, and Q. Wang. Numerical approximations for the molecular beam epitaxial growth model based on the invariant energy quadratization method. *Journal of Computational Physics*, 333:102–127, 2017.
[55] X. Yang, J. Zhao, Q. Wang, and J. Shen. Numerical approximations for a three components Cahn-Hilliard phase-field model based on the invariant energy quadratization method. *Mathematical Models and Methods in Applied Sciences*, 27:1993–2023, 2017.
[56] H. Yu and X. Yang. Numerical approximations for a phase-field moving contact line model with variable densities and viscosities. *Journal of Computational Physics*, 334:665–686, 2017.
[57] J. Zhao. A revisit of the energy quadratization method with a relaxation technique. *Applied Mathematics Letters*, 120:107331, 2021.
[58] J. Zhao, X. Yang, Y. Gong, and Q. Wang. A novel linear second order unconditionally energy stable scheme for a hydrodynamic Q-tensor model of liquid crystals. *Computer Methods in Applied Mechanics and Engineering*, 318:803–825, 2017.
[59] J. Zhao, X. Yang, Y. Gong, X. Zhao, X. Yang, J. Li, and Q. Wang. A general strategy for numerical approximations of non-equilibrium models–part i thermodynamical systems. *International Journal of Numerical Analysis and Modeling*, 15(6):884–918, 2018.
[60] J. Zhu, L. Q. Chen, J. Shen, and V Tikare. Coarsening kinetics from a variable-mobility Cahn-Hilliard equation: Application of a semi-implicit Fourier spectral method. *Physical Review E*, 60(4):3564, 1999.